

This discussion paper is/has been under review for the journal Geoscientific Model Development (GMD). Please refer to the corresponding final paper in GMD if available.

A semi-implicit, second order accurate numerical model for multiphase underexpanded volcanic jets

S. Carcano¹, L. Bonaventura¹, T. Esposti Ongaro², and A. Neri²

¹MOX – Modelling and Scientific Computing, Dipartimento di Matematica “F. Brioschi”, Politecnico di Milano, Via Bonardi 9, 20133 Milano, Italy

²Istituto Nazionale di Geofisica e Vulcanologia, Sezione di Pisa, Via della Faggiola 32, 56126 Pisa, Italy

Received: 21 December 2012 – Accepted: 2 January 2013 – Published: 22 January 2013

Correspondence to: S. Carcano (susanna.carcano@mail.polimi.it)

Published by Copernicus Publications on behalf of the European Geosciences Union.

GMDD

6, 399–452, 2013

A numerical model
for volcanic jets

S. Carcano et al.

[Title Page](#)

[Abstract](#)

[Introduction](#)

[Conclusions](#)

[References](#)

[Tables](#)

[Figures](#)

◀

▶

◀

▶

[Back](#)

[Close](#)

[Full Screen / Esc](#)

[Printer-friendly Version](#)

[Interactive Discussion](#)



Abstract

An improved version of the PDAC (Pyroclastic Dispersal Analysis Code, Esposti Ongaro et al., 2007) numerical model for the simulation of multiphase volcanic flows is presented and validated for the simulation of multiphase volcanic jets in supersonic regimes. The present version of PDAC includes second-order time and space discretizations and fully multidimensional advection discretizations, in order to reduce numerical diffusion and enhance the accuracy of the original model. The model is tested on the problem of jet decompression, in both two and three dimensions. For homogeneous jets, numerical results are consistent with experimental results at the laboratory scale (Lewis and Carlson, 1964). For non-equilibrium gas-particle jets, we consider monodisperse and bidisperse mixtures and we quantify non-equilibrium effects in terms of the ratio between the particle relaxation time and a characteristic jet time scale. For coarse particles and low particle load, numerical simulations well reproduce laboratory experiments and numerical simulations carried out with an Eulerian-Lagrangian model (Sommerfeld, 1993). At the volcanic scale, we consider steady-state conditions associated to the development of Vulcanian and sub-Plinian eruptions. For the finest particles produced in these regimes, we demonstrate that the solid phase is in mechanical and thermal equilibrium with the gas phase and that the jet decompression structure is well described by a pseudogas model (Ogden et al., 2008). Coarse particles, on the contrary, display significant non-equilibrium effects, associated to their larger relaxation time. Deviations from the equilibrium regime occur especially during the rapid acceleration phases and are able to appreciably modify the average jet dynamics, with maximum velocity and temperature differences of the order of 150 m s^{-1} and 80 K across shock waves.

A numerical model for volcanic jets

S. Carcano et al.

[Title Page](#)

[Abstract](#)

[Introduction](#)

[Conclusions](#)

[References](#)

[Tables](#)

[Figures](#)

[◀](#)

[▶](#)

[◀](#)

[▶](#)

[Back](#)

[Close](#)

[Full Screen / Esc](#)

[Printer-friendly Version](#)

[Interactive Discussion](#)



1 Introduction

During explosive volcanic eruptions a mixture of gases, magma fragments, crystals and eroded rocks is injected in the atmosphere at high velocity, pressure and temperature. The diverse and unpredictable variability of eruptive styles depends mostly on the complex rheology of magma and the nonlinear processes leading to the fragmentation of the viscous melt into a polydisperse mixture of gases and particles (Gonnermann and Manga, 2007). Nonetheless, the explosive character of an eruption is always associated to the rapid decompression and the consequent abrupt expansion of gases in the magma (the exsolved magmatic volatiles in magmatic eruptions, vaporized free water or hydrothermal fluids in hydromagmatic and phreatomagmatic eruptions) (Parfitt and Wilson, 2008). Under such conditions, in the proximity of the volcanic vent, the erupted underexpanded multiphase mixture can manifest the features of supersonic flows (Kieffer, 1984; Woods and Bower, 1995; Esposti Ongaro et al., 2008; Ogden et al., 2008b; Orescanin et al., 2010), which, in turn, directly affect the plume source conditions. After decompression, column behaviour is controlled by the balance between its negative buoyancy, associated to the load of solid particles, and the positive buoyancy due to air heating and expansion. Plume dynamics is therefore mainly influenced by (subsonic) turbulent mixing and mass and thermal exchange between the eruptive mixture and the atmosphere. Depending upon the efficiency of the turbulent entrainment the gas-particle mixture can form a buoyant plume in the atmosphere or collapse under its particle load forming pyroclastic density currents (Valentine, 1998).

A general understanding of the transport dynamics of pyroclasts in the atmosphere has been first achieved by describing the eruptive mixture as homogeneous, i.e. by assuming kinetic and thermal equilibrium between gas and particles and by solving the resulting transport equations under simplified conditions (e.g. one-dimensional and steady state approximations) (Wilson, 1976; Woods, 1988; Sparks et al., 1997). Such approach has also been extended to two and three dimensions and transient regime (Oberhuber et al., 1998; Suzuki et al., 2005; Ogden et al., 2008a), to carry

A numerical model for volcanic jets

S. Carcano et al.

[Title Page](#)

[Abstract](#)

[Introduction](#)

[Conclusions](#)

[References](#)

[Tables](#)

[Figures](#)

[◀](#)

[▶](#)

[◀](#)

[▶](#)

[Back](#)

[Close](#)

[Full Screen / Esc](#)

[Printer-friendly Version](#)

[Interactive Discussion](#)



out numerical simulations of volcanic processes at the large scale, highlighting the key roles of environmental atmospheric conditions (Graf et al., 1999), large-eddy turbulence (Suzuki and Koyaguchi, 2010), vent overpressure (Ogden et al., 2008b) and boundary-layer processes (Doronzo et al., 2012).

5 However, the detailed reconstruction of well documented eruptions and the growing need to quantify and map the hazards associated to future explosive events require the simulation of full eruptive scenarios. To this aim, eruption models able to incorporate the main dynamic processes and more realistic input conditions are needed. The problem, in its general multidimensional and unsteady formulation, is extremely challenging due
10 to the multiphase nature of the flow and to its multiscale features.

Mathematical models based on multiphase flow formulation have been proposed starting from the late 1980's (Valentine and Wohletz, 1989; Dobran et al., 1993) but have become more popular in the last decade (Dartevelle et al., 2004; Pelanti and LeVeque, 2006; Dufek and Bergantz, 2007; Esposti Ongaro et al., 2007) also thanks to the
15 impressive development of computational techniques allowing the solution of the complicated set of transport equations on modern high-performance parallel computers.

This work is based on the application and enhancement of the PDAC model, (Pyroclastic Dispersal Analysis Code), described in Sect. 2 and in more detail in Neri et al. (2003) and Esposti Ongaro et al. (2007), able to solve the multiphase flow
20 equations for a mixture of volcanic gases and pyroclasts in non-equilibrium conditions and exchanging momentum and heat. The PDAC numerical solution procedure is based on the original algorithm by Harlow and Amsden (1975), in which a first order semi-implicit treatment for multiphase flows was combined with simple, donor cell based finite volume conservative advection schemes. Typically, such first-order techniques
25 introduce large amounts of numerical diffusion. Esposti Ongaro et al. (2007) extended the first-order spatial discretization to second order in each separate spatial direction, by adopting the one-dimensional MUSCL scheme (Sweby, 1984), as common practice in other multiphase flow codes (e.g. MFIX in Syamlal et al., 1993; Syamlal, 1998), but did not modify the semi-implicit time-advancement scheme based on the

A numerical model for volcanic jets

S. Carcano et al.

[Title Page](#)

[Abstract](#)

[Introduction](#)

[Conclusions](#)

[References](#)

[Tables](#)

[Figures](#)

◀

▶

◀

▶

[Back](#)

[Close](#)

[Full Screen / Esc](#)

[Printer-friendly Version](#)

[Interactive Discussion](#)



backward Euler discretization of time derivatives. The resulting numerical method was effective, but its results still display significant numerical diffusion, especially in multi-dimensional simulations, which implies the need for very high spatial resolution and small time-steps to achieve an accurate simulation.

5 The objective of this work is to modify the numerical algorithm in order to make it more suitable to the resolution of the near-vent decompression dynamics, potentially involving supersonic regimes and shock waves, and the three-dimensional, transient dynamics of turbulent eddies, controlling, for example, the atmospheric air entrainment. We propose an improvement of the original PDAC numerical model to achieve higher
10 accuracy and robustness in the resolution of compressible regimes, while reducing the numerical diffusion that may significantly damp turbulent eddies in subsonic regimes. More specifically, a second order Crank–Nicolson type time discretization (Crank and Nicolson, 1947) and a more accurate and fully multidimensional advection scheme (LeVeque, 1996) are introduced in the framework of the semi-implicit approach proposed
15 by Harlow and Amsden (1975).

The resulting model is applied to the simulation of the decompression structures that form in the lower portion of volcanic columns and is validated against laboratory experiments and by comparison with other model results. Although in the context of volcanic eruption simulations a rigorous model verification or validation are not possible (Oreskes et al., 1994), three-dimensional multiphase flow models have demonstrated, in the last years, the potential for providing a good representation of the actual processes occurring in the real system (Dufek and Bergantz, 2007; Esposti Ongaro et al., 2012). The validation of numerical results against empirical observations of well-documented eruptions, together with the congruence of numerical benchmarks with
20 experimental and theoretical results, are at present the only available instruments to assess the “empirical adequacy” (Oreskes et al., 1994) of models to simulate eruptive scenarios. As it will be shown below, the results of the present model are in good qualitative and quantitative agreement with a number of experimental and numerical results available in the literature.

A numerical model for volcanic jets

S. Carcano et al.

[Title Page](#)

[Abstract](#)

[Introduction](#)

[Conclusions](#)

[References](#)

[Tables](#)

[Figures](#)

[◀](#)

[▶](#)

[◀](#)

[▶](#)

[Back](#)

[Close](#)

[Full Screen / Esc](#)

[Printer-friendly Version](#)

[Interactive Discussion](#)



In Sect. 2, we describe briefly the PDAC model and the simplifying assumption adopted in the present work. In Sects. 3 and 4, the present, improved version of the PDAC numerical method is described. Numerical benchmarks and comparison with analogous results obtained with other models are presented in Sect. 5. Finally, some
5 conclusions and perspectives for future work are presented in Sect. 6.

2 Multiphase flow equations

In this work we employ the same model equations as in the original PDAC model proposed by Neri et al. (2003). They are appropriate to describe the injection and dispersal of a hot and high velocity gas-pyroclast mixture in a standard reference atmosphere.

10 The model is based on the following main hypotheses:

- the solid particles and the gas are considered as interpenetrating continua, following an Eulerian-Eulerian approach;
- the gas phase is compressible and obeys the ideal gas law;
- mass transfer processes due to phase changes and chemical reactions are neglected;
- solid particles are assumed to be spherical and each class is assumed to consist of particles of equal radius and density;
- particles are assumed to maintain their original size, thus neglecting the effect of any secondary fragmentation or aggregation process on the large-scale dispersal dynamics;
- the heat transfer between different solid phases, as well as the viscous dissipation effects, are neglected due to their second-order effect in comparison with advection, conduction and gas-particle heat exchange.

[Title Page](#)

[Abstract](#)

[Introduction](#)

[Conclusions](#)

[References](#)

[Tables](#)

[Figures](#)

◀

▶

[Back](#)

[Close](#)

[Full Screen / Esc](#)

[Printer-friendly Version](#)

[Interactive Discussion](#)



A numerical model for volcanic jets

S. Carcano et al.

[Title Page](#)[Abstract](#)[Introduction](#)[Conclusions](#)[References](#)[Tables](#)[Figures](#)[◀](#)[▶](#)[◀](#)[▶](#)[Back](#)[Close](#)[Full Screen / Esc](#)[Printer-friendly Version](#)[Interactive Discussion](#)

While in general turbulence and other dissipative effects cannot be neglected, in this study, for the sake of simplicity, we only focus on inviscid equations and regimes. As reported in detail in Carcano et al. (2012), a scaling analysis of the model equations shows that the typical values of the Reynolds number $Re = \frac{\rho UL}{\mu}$ and the Péclet number

$Pe = \frac{c_p \rho UL}{k}$ (based on diameter and velocity at the vent and on average mixture properties) in a volcanic jet vary from 10^6 to 10^{11} in the regimes of interest. Consequently, the only dissipative terms retained in the following are those representing interphase exchange processes between the gas and the solid phase. However, all the physical processes neglected in this study are actually accounted for in the complete PDAC model, in the same way as in the original model proposed in Neri et al. (2003), to which we refer for a more complete description of these terms.

The gas phase is composed of different chemical components leaving the crater, such as water vapor and carbon dioxide, and atmospheric air, considered as a single chemical component. The pyroclasts are described by N classes of solid particles, each one characterized by a diameter, density, specific heat and thermal conductivity. In the following sections, we will denote with the subscript $s = 1 \dots N$ the classes of solid particles and with $l = 1 \dots M$ the chemical components of the gas phase g . The model variables can be defined as follows:

- ϵ_g, ϵ_s = volumetric fractions of gas and solid particles; if V is the representative volume and V_g and V_s are the volumes occupied by gas and particles, respectively, the gas and solid volume fractions are defined by $\epsilon_g = V_g/V$, $\epsilon_s = V_s/V$;
- ρ_g, ρ_s = microscopic densities of gas and solid particles;
- y_l = mass fractions of the gas components;
- $\mathbf{v}_g, \mathbf{v}_s$ = velocities of gas and solid particles;
- p_g = gas pressure;
- h_g, h_s = enthalpies of gas and solid particles;

A numerical model for volcanic jets

S. Carcano et al.

[Title Page](#)

[Abstract](#)

[Introduction](#)

[Conclusions](#)

[References](#)

[Tables](#)

[Figures](#)

◀

▶

◀

▶

[Back](#)

[Close](#)

[Full Screen / Esc](#)

[Printer-friendly Version](#)

[Interactive Discussion](#)



– T_g, T_s = temperatures of gas and solid particles.

The model consists of $5(N + 1) + M$ coupled partial differential equations for the independent variables $\rho_g, \rho_s, \epsilon_s, \mathbf{v}_s, h_s$ (or T_s), y_l , with $s = g, 1 \dots N$ and $l = 1 \dots M$. The mass conservation equations for the gas phase g , the s -th solid phase and the l -th gas chemical component are

$$\frac{\partial(\epsilon_g \rho_g)}{\partial t} + \nabla \cdot (\epsilon_g \rho_g \mathbf{v}_g) = 0, \quad (1)$$

$$\frac{\partial(\epsilon_s \rho_s)}{\partial t} + \nabla \cdot (\epsilon_s \rho_s \mathbf{v}_s) = 0, \quad s = 1 \dots N, \quad (2)$$

$$\frac{\partial(\epsilon_l \rho_l y_l)}{\partial t} + \nabla \cdot (\epsilon_l \rho_l y_l \mathbf{v}_g) = 0, \quad l = 1 \dots M. \quad (3)$$

The momentum balance equations for the gas phase and the s -th solid phase, for all $s = 1 \dots N$ are written as

$$\frac{\partial(\epsilon_g \rho_g \mathbf{v}_g)}{\partial t} + \nabla \cdot (\epsilon_g \rho_g \mathbf{v}_g \mathbf{v}_g) = -\epsilon_g \nabla p_g + \epsilon_g \rho_g \mathbf{g} + \sum_{s=1}^N D_{s,g} (\mathbf{v}_s - \mathbf{v}_g), \quad (4)$$

$$\frac{\partial(\epsilon_s \rho_s \mathbf{v}_s)}{\partial t} + \nabla \cdot (\epsilon_s \rho_s \mathbf{v}_s \mathbf{v}_s) = -\epsilon_s \nabla p_g + \epsilon_s \rho_s \mathbf{g} + \sum_{p=1}^N D_{p,s} (\mathbf{v}_p - \mathbf{v}_s) + D_{g,s} (\mathbf{v}_g - \mathbf{v}_s). \quad (5)$$

(with $p \neq s$). Here, $D_{p,s}$ represents the drag coefficient describing the interaction between the phase p and the phase s and \mathbf{g} denotes the gravitational acceleration vector. In the present formulation, we adopted Model A by Gidaspow (1994), in which the gas pressure gradient is present in both of gas and particles momentum equations. Numerical experiments assuming a pressureless particulate phase (Model B) do not show significant differences, at least in the dilute regime under investigation. The energy balance equations for the gas phase and the solid phases $s = 1 \dots N$ are written

in terms of their enthalpies:

$$\frac{\partial(\epsilon_g \rho_g h_g)}{\partial t} + \nabla \cdot (\epsilon_g \rho_g h_g \mathbf{v}_g) = \epsilon_g \left(\frac{\partial p_g}{\partial t} + \mathbf{v}_g \cdot \nabla p_g \right) + \sum_{s=1}^N Q_s (T_s - T_g), \quad (6)$$

$$\frac{\partial(\epsilon_s \rho_s h_s)}{\partial t} + \nabla \cdot (\epsilon_s \rho_s h_s \mathbf{v}_s) = Q_s (T_g - T_s). \quad (7)$$

5 Here, Q_s is the volumetric heat transfer rate between the gas and the s -th solid phase. For the gas phase, we have considered the reversible rate of enthalpy change due to compression or expansion, which is important in transient, compressible flows. Heat transfer between different solid phases is negligible, and also radiative heat transfer has not been considered. As remarked before, viscous dissipation has been neglected
10 for the applications considered in this paper, based on the results of the scale analysis.

By definition of the volumetric and mass fractions, one also has the relations

$$\epsilon_g + \sum_{s=1}^N \epsilon_s = 1, \quad 0 \leq \epsilon_g \leq 1, \quad 0 \leq \epsilon_s \leq 1, \quad (8)$$
$$\sum_{l=1}^M y_l = 1, \quad 0 \leq y_l \leq 1.$$

15 The gas phase is compressible and we suppose that thermodynamic quantities are related by the ideal gas law:

$$p_g = \tilde{R} \rho_g T_g, \quad (9)$$

20 where \tilde{R} is the gas constant of the mixture of gaseous components. Particulate solid phases are considered incompressible. Consequently, their microscopic density is assumed to be constant and denoted by ρ_s , $s = 1 \dots N$. The temperature of each phase

[Title Page](#)

[Abstract](#)

[Introduction](#)

[Conclusions](#)

[References](#)

[Tables](#)

[Figures](#)

[◀](#)

[▶](#)

[◀](#)

[▶](#)

[Back](#)

[Close](#)

[Full Screen / Esc](#)

[Printer-friendly Version](#)

[Interactive Discussion](#)



is derived from its enthalpy as:

$$T_s = \frac{h_s}{c_{p,s}}, \quad s = g, 1 \dots N, \quad (10)$$

where particle specific heats $c_{p,s}$ are assumed to be constant and to correspond to average values, due to their minor sensitivity on temperature. The specific heat of the gas phase $c_{p,g}$ depends on temperature and it is computed as a weighted average of the specific heats of the M chemical components:

$$c_{p,g} = \sum_{l=1}^M y_l c_{p,l}. \quad (11)$$

Interphase drag coefficients and heat transfer rates are derived from semi-empirical correlations for dilute and dense regimes.

The initial values of all field variables must be specified for the entire computational domain. Usually, a standard atmosphere, vertically stratified in pressure, temperature and density, is considered throughout the domain. The atmosphere is composed of dry air at rest and no particle of any size is considered present in the computational domain. Appropriate boundary conditions will be described later for each specific test case.

3 The numerical method: semi-implicit time discretization

The model equations described in the previous section are discretized in time by a second order version of the implicit multifield (IMF) algorithm proposed in Harlow and Amsden (1975). We will describe the time discretization method in the simpler case of a single solid phase s . We employ a semi-implicit time discretization based on a Crank–Nicolson type time averaging (also known as θ -method) with averaging parameter $\theta \in [0, 1]$ (Crank and Nicolson, 1947). It is well known (see e.g. Quarteroni

[Title Page](#)

[Abstract](#)

[Introduction](#)

[Conclusions](#)

[References](#)

[Tables](#)

[Figures](#)

◀

▶

◀

▶

[Back](#)

[Close](#)

[Full Screen / Esc](#)

[Printer-friendly Version](#)

[Interactive Discussion](#)



et al., 2002) that, for unconditional linear stability, one has to choose $\theta \geq 1/2$, while full second order accuracy is only granted for the limit value $\theta = 1/2$.

The continuity equation for the phase s is discretized as:

$$_5 (\epsilon_s \rho_s)^{n+1} + \theta \Delta t [\nabla \cdot (\epsilon_s \rho_s \mathbf{v}_s)]^{n+1} = (\epsilon_s \rho_s)^n - (1 - \theta) \Delta t [\nabla \cdot (\epsilon_s \rho_s \mathbf{v}_s)]^n. \quad (12)$$

The momentum equation for the phase s , with $p \neq s$ is discretized as:

$$\begin{aligned} & (\epsilon_s \rho_s \mathbf{v}_s)^{n+1} + \theta \Delta t [\epsilon_s \nabla p_g - D_{p,s}^n (\mathbf{v}_p - \mathbf{v}_s) - \epsilon_s \rho_s \mathbf{g}]^{n+1} \\ & = (\epsilon_s \rho_s \mathbf{v}_s)^n - \Delta t [\nabla \cdot (\epsilon_s \rho_s \mathbf{v}_s \mathbf{v}_s)]^n + (1 - \theta) \Delta t [-\epsilon_s \nabla p_g + D_{p,s}^n (\mathbf{v}_p - \mathbf{v}_s) + \epsilon_s \rho_s \mathbf{g}]^n. \end{aligned} \quad (13)$$

10 Notice that the pressure, the gravity and the drag terms are discretized in time by the θ -method, while flux terms are treated explicitly. The enthalpy equations for the gas phase g and the solid phase s are solved after continuity and momentum equations. Only the interphase exchange terms are treated semi-implicitly by the θ -method, while convective terms are treated explicitly, by using the updated densities and velocities.

$$\begin{aligned} & _{15} (\epsilon_g \rho_g h_g)^{n+1} - \theta \Delta t Q_s^n [T_s - T_g]^{n+1} = (\epsilon_g \rho_g)^{n+1} h_g^n + (1 - \theta) \Delta t Q_s^n [T_s - T_g]^n \\ & - \Delta t [\nabla \cdot (\epsilon_g^{n+1} \rho_g^{n+1} h_g^n \mathbf{v}_g^{n+1})] + \Delta t \left[\epsilon_g^{n+1} \left(\frac{p_g^{n+1} - p_g^n}{\Delta t} + \mathbf{v}_g^{n+1} \cdot \nabla p_g^{n+1} \right) \right], \end{aligned} \quad (14)$$

$$\begin{aligned} & (\epsilon_s \rho_s h_s)^{n+1} - \theta \Delta t Q_s^n [T_g - T_s]^{n+1} \\ & = (\epsilon_s \rho_s)^{n+1} h_s^n + (1 - \theta) \Delta t Q_s^n [T_g - T_s]^n - \Delta t [\nabla \cdot (\epsilon_s^{n+1} \rho_s^{n+1} h_s^n \mathbf{v}_s^{n+1})]. \end{aligned} \quad (15)$$

[Title Page](#)

[Abstract](#)

[Introduction](#)

[Conclusions](#)

[References](#)

[Tables](#)

[Figures](#)

[◀](#)

[▶](#)

[◀](#)

[▶](#)

[Back](#)

[Close](#)

[Full Screen / Esc](#)

[Printer-friendly Version](#)

[Interactive Discussion](#)



The whole set of equations can be reformulated as

$$\begin{aligned} (\epsilon_g \rho_g)^{n+1} + \theta \Delta t [\nabla \cdot (\epsilon_g \rho_g \mathbf{v}_g)]^{n+1} &= \mathcal{E}_{\rho_g}^n, \\ (\epsilon_s \rho_s)^{n+1} + \theta \Delta t [\nabla \cdot (\epsilon_s \rho_s \mathbf{v}_s)]^{n+1} &= \mathcal{E}_{\rho_s}^n, \\ (\epsilon_g \rho_g \mathbf{v}_g)^{n+1} + \theta \Delta t \left[\epsilon_g \nabla p_g - D_{g,s}^n (\mathbf{v}_s - \mathbf{v}_g) - \epsilon_g \rho_g \mathbf{g} \right]^{n+1} &= \mathcal{E}_{\mathbf{v}_g}^n, \\ (\epsilon_s \rho_s \mathbf{v}_s)^{n+1} + \theta \Delta t \left[\epsilon_s \nabla p_g - D_{g,s}^n (\mathbf{v}_g - \mathbf{v}_s) - \epsilon_s \rho_s \mathbf{g} \right]^{n+1} &= \mathcal{E}_{\mathbf{v}_s}^n, \\ (\epsilon_g \rho_g h_g)^{n+1} - \theta \Delta t Q_s^n [T_s - T_g]^{n+1} &= \mathcal{E}_{h_g}^n, \\ (\epsilon_s \rho_s h_s)^{n+1} - \theta \Delta t Q_s^n [T_g - T_s]^{n+1} &= \mathcal{E}_{h_s}^n, \end{aligned} \quad (16)$$

where the \mathcal{E} terms include all the explicit terms.

5 For each time step t^{n+1} , Eq. (16) are solved by this second order extension of the IMF algorithm as follows:

- temperature dependent coefficients of the gas phase are computed;
- the interphase coefficients $D_{g,s}$ and Q_s and the explicit \mathcal{E} terms are computed;
- the coupled continuity and momentum equations are solved iteratively to update velocity fields, pressure and volumetric fractions;
- 10 gas mass fractions y_i are computed by solving the linear transport equations;
- the energy equations are solved explicitly for all phases (the system is linear in the temperatures).

15 We observe that, since the enthalpy equations are solved explicitly after the solution of the momentum and continuity equations, the temperature is kept constant during the solution procedure. The effect of the temperature variation on the gas pressure and density are deferred to the next time-step computation.

[Title Page](#)

[Abstract](#)

[Introduction](#)

[Conclusions](#)

[References](#)

[Tables](#)

[Figures](#)

[◀](#)

[▶](#)

[◀](#)

[▶](#)

[Back](#)

[Close](#)

[Full Screen / Esc](#)

[Printer-friendly Version](#)

[Interactive Discussion](#)



4 The numerical method: space discretization

The model equations are discretized by a finite volume approach on an orthogonal, non uniform mesh. A staggered discretization grid with $N_x \times N_y \times N_z$ Cartesian cells is introduced, along the lines of popular discretization methods such as the MAC (marker and cell) approach, introduced in Harlow and Welch (1965), or the Arakawa C grid (see e.g. Arakawa and Lamb, 1981). The mesh is composed by rectangular control volumes obtained from the cartesian product of three 1-D discretization intervals along each axis. Each cell is numbered at its center with indices i , j and k , for the x, y and z directions, respectively. If we denote by $i = 1 \dots N_x$, $j = 1 \dots N_y$, $k = 1 \dots N_z$ the intervals along the x, y and z axis, respectively, the center of each cell can be identified by a triplet of indices (i, j, k) . The length of the cell sides in each directions are denoted by Δx_i , Δy_j and Δz_k and they are assumed to vary in their respective direction only. The cell volume is given by $V_{i,j,k} = \Delta x_i \Delta y_j \Delta z_k$ and staggered spacings $\Delta x_{i+\frac{1}{2}}$ are defined as the arithmetic average of the neighboring, integer index values.

The discrete u velocity is defined at half integer i and integers j and k , v is defined at integers i , k and half integer j , while w is defined at integers i, j and half integers k . Finally, p and all other three-dimensional scalar variables, i.e. pressure, densities, volumetric fractions and enthalpies, are defined at integers i, j, k . Therefore mass and enthalpy equations are solved on the cell centers, whereas the momentum equations are solved at the staggered locations. At points where they are not defined, the discrete variables are generally computed by linear interpolation of the nearest values. Averaged quantities will usually be denoted by an overbar. On a uniform grid, for example:

$$\bar{u}_{i,j,k} = \frac{u_{i+\frac{1}{2},j,k} + u_{i-\frac{1}{2},j,k}}{2}, \quad (17)$$
$$\bar{u}_{i,j+\frac{1}{2},k} = \frac{u_{i+\frac{1}{2},j,k} + u_{i-\frac{1}{2},j,k} + u_{i+\frac{1}{2},j+1,k} + u_{i-\frac{1}{2},j+1,k}}{4}.$$

25

GMDD

6, 399–452, 2013

A numerical model for volcanic jets

S. Carcano et al.

[Title Page](#)[Abstract](#)[Introduction](#)[Conclusions](#)[References](#)[Tables](#)[Figures](#)[◀](#)[▶](#)[◀](#)[▶](#)[Back](#)[Close](#)[Full Screen / Esc](#)[Printer-friendly Version](#)[Interactive Discussion](#)

If we denote with brackets $\langle \dots \rangle$ the discretization of the advective fluxes and we adopt the staggered approach described above, we obtain, for both the gas phase and the solid phase, for each cell (i, j, k) of the mesh, the following system of discretized equations:

$$5 \quad (\epsilon_s \rho_s)_{ijk}^{n+1} + \theta \left[\frac{\Delta t}{\Delta x} \langle \epsilon_s \rho_s \bar{u}_s \rangle_{ijk}^{n+1} + \frac{\Delta t}{\Delta y} \langle \epsilon_s \rho_s \bar{v}_s \rangle_{ijk}^{n+1} + \frac{\Delta t}{\Delta z} \langle \epsilon_s \rho_s \bar{w}_s \rangle_{ijk}^{n+1} \right] = \mathcal{E}_{\rho_s,ijk}^n, \quad (18)$$

$$(\bar{\epsilon}_s \bar{\rho}_s u_s)_{i+\frac{1}{2}jk}^{n+1} + \theta \frac{\Delta t}{\Delta x} \bar{\epsilon}_{s,i+\frac{1}{2}jk}^{n+1} (p_{g,i+1jk}^{n+1} - p_{g,ijk}^{n+1}) \\ - \theta \Delta t D_{ps,i+\frac{1}{2}jk}^n \left(u_{p,i+\frac{1}{2}jk}^{n+1} - u_{s,i+\frac{1}{2}jk}^{n+1} \right) - \theta \Delta t [\bar{\epsilon}_s \bar{\rho}_s g_x]_{i+\frac{1}{2}jk}^{n+1} = \mathcal{E}_{u_s,i+\frac{1}{2}jk}^n, \quad (19)$$

$$(\bar{\epsilon}_s \bar{\rho}_s v_s)_{ij+\frac{1}{2}k}^{n+1} + \theta \frac{\Delta t}{\Delta y} \bar{\epsilon}_{s,ij+\frac{1}{2}k}^{n+1} (p_{g,ij+1k}^{n+1} - p_{g,ijk}^{n+1}) \\ - \theta \Delta t D_{ps,ij+\frac{1}{2}k}^n \left(v_{p,ij+\frac{1}{2}k}^{n+1} - v_{s,ij+\frac{1}{2}k}^{n+1} \right) - \theta \Delta t [\bar{\epsilon}_s \bar{\rho}_s g_y]_{ij+\frac{1}{2}k}^{n+1} = \mathcal{E}_{v_s,ij+\frac{1}{2}k}^n, \quad (20)$$

$$(\bar{\epsilon}_s \bar{\rho}_s w_s)_{ijk+\frac{1}{2}}^{n+1} + \theta \frac{\Delta t}{\Delta z} \bar{\epsilon}_{s,ijk+\frac{1}{2}}^{n+1} (p_{g,ijk+1}^{n+1} - p_{g,ijk}^{n+1}) \\ - \theta \Delta t D_{ps,ijk+\frac{1}{2}}^n \left(w_{p,ijk+\frac{1}{2}}^{n+1} - w_{s,ijk+\frac{1}{2}}^{n+1} \right) - \theta \Delta t [\bar{\epsilon}_s \bar{\rho}_s g_z]_{ijk+\frac{1}{2}}^{n+1} = \mathcal{E}_{w_s,ijk+\frac{1}{2}}^n, \quad (21)$$

$$10 \quad (\epsilon_s \rho_s h_s)_{ijk}^{n+1} - \theta \Delta t Q_{s,ijk}^n [T_p - T_s]_{ijk}^{n+1} = \mathcal{E}_{h_s,ijk}^n, \quad (22)$$

for all $s, p = g, 1 \dots N$ and $p \neq s$, where the discretization of the \mathcal{E} -terms is specified in Appendix B. The \mathcal{E} -terms are computed explicitly before the resolution of the system.

Finally, we introduce an appropriate discretization technique for the advective fluxes. From the nondimensional analysis (Carcano et al., 2012), we know that advection is one of the dominating phenomena in the process, so we expect that a proper numerical treatment of the advection terms should be necessary in order to obtain an accurate numerical solution. Therefore, a first possible modification of the donor-cell scheme is to introduce in the upwind discretization the so-called transverse fluxes (Colella,

[Title Page](#)
[Abstract](#)
[Introduction](#)
[Conclusions](#)
[References](#)
[Tables](#)
[Figures](#)
[◀](#)
[▶](#)
[◀](#)
[▶](#)
[Back](#)
[Close](#)
[Full Screen / Esc](#)
[Printer-friendly Version](#)
[Interactive Discussion](#)


A numerical model
for volcanic jets

S. Carcano et al.

[Title Page](#)[Abstract](#)[Introduction](#)[Conclusions](#)[References](#)[Tables](#)[Figures](#)[◀](#)[▶](#)[◀](#)[▶](#)[Back](#)[Close](#)[Full Screen / Esc](#)[Printer-friendly Version](#)[Interactive Discussion](#)

1990; Saltzman, 1993; LeVeque, 1996). In the standard donor-cell upwind method, the advective flux through one single cell boundary is split into independent fluxes along the x-, y- and z-directions by using the velocities u , v and w in the directions normal to each interface. More accurate methods can be obtained by considering the flux with the

5 proper speed $\mathbf{v} = (u, v, w)$, without splitting it along the three space directions. Unsplit upwind schemes are more accurate (in particular, less diffusive) and more stable than the original donor-cell upwind method.

This improved version of the upwind method is called the Corner Transport Upwind (CTU) method (Colella, 1990). A hierarchy of methods for the numerical solution of advective transport in conservation equations in several space dimensions based on CTU 10 has been proposed by LeVeque (1996). In the present model, we employ one of the second order versions of the algorithm described in LeVeque (1996), including *minmod* flux limiting (Roe, 1986) to avoid the creation of spurious extrema in the solution.

15 As an example, in the simpler two-dimensional case, the advective flux $\langle Qu \rangle_{ik}$ of the scalar quantity Q along the x-direction in the computational cell (i, k) is computed as

$$\langle Qu \rangle_{ik} = (Qu)_{i+\frac{1}{2}k} - (Qu)_{i-\frac{1}{2}k} \quad (23)$$

For $u_{ik-\frac{1}{2}} > 0$ and $w_{ik-\frac{1}{2}} > 0$ we compute

$$\begin{aligned} (Qu)_{i+\frac{1}{2}} &= Q_{ik} u_{i+\frac{1}{2}k} - \frac{1}{2} u_{ik-\frac{1}{2}} w_{ik-\frac{1}{2}} (Q_{ik} - Q_{ik-1}) \\ &+ \frac{1}{2} u_{i+\frac{1}{2}k} \left(1 - \frac{\Delta t}{\Delta x} u_{i+\frac{1}{2}k} \right) (Q_{i+1k} - Q_{ik}) \cdot \text{lim} \end{aligned} \quad (24)$$

20 where lim represents the flux limiter. Analogous expressions are written for $u_{ik-\frac{1}{2}} < 0$ and/or $w_{ik-\frac{1}{2}} < 0$. The first term on the right hand side represent the donor-cell upwind flux, the second term represents the Corner Transport Upwind correction, whereas the last term represents its second order extension.

5 Model validation: axisymmetric underexpanded jet

The proposed numerical method has been tested on two- and three-dimensional simulations of underexpanded jets and the numerical results obtained have been compared with both experimental and numerical results available in the literature. In order to simulate a cylindrical underexpanded jet, we assume that each phase enters the domain through a fixed inlet where the volume fraction, velocity and temperature of each phase and the gas pressure are imposed. Mechanical and thermal equilibrium between the phases at the vent are assumed. In two-dimensional tests, we solve the model equations in cylindrical coordinates and we impose symmetry conditions at the left lateral boundary. At the bottom boundary, no mass and heat transfer are allowed and free-slip conditions are assumed for the velocity of each phase. At the upper boundary, free outflow/inflow conditions are assumed, whereas at the lateral boundaries it is possible to assume either free-slip or free outflow/inflow conditions. In particular, at the outflow boundaries, the mass and momentum equations of the mixture are solved for pressure, assuming a null velocity gradient along the boundary. At the lateral inflow boundaries, incoming air is assumed to be free of particles and to have pressure and temperature characteristics corresponding to those of the standard reference atmosphere.

5.1 Comparison with laboratory results and empirical laws

We present here a set of numerical tests aimed at the simulation of pure gas and gas-particles jets at the laboratory scale. It has been proven theoretically and experimentally that vents with supersonic or sonic vertical velocity and gas pressure greater than the atmospheric one result in a rapid expansion and acceleration of the fluid to high Mach number (Lewis and Carlson, 1964). A series of expansion waves form at the vent exit (Prandtl-Meyer expansion), which are reflected as compression waves at the jet flow boundary. The compression waves coalesce to form a barrel shock and a standing normal shock wave (Mach disk), across which the vertical velocity is reduced and the pressure in the core of the jet increases. The fluid that crosses the Mach disk is

A numerical model for volcanic jets

S. Carcano et al.

[Title Page](#)

[Abstract](#)

[Introduction](#)

[Conclusions](#)

[References](#)

[Tables](#)

[Figures](#)

◀

▶

◀

▶

[Back](#)

[Close](#)

[Full Screen / Esc](#)

[Printer-friendly Version](#)

[Interactive Discussion](#)



rapidly compressed and decelerated to subsonic speeds. Above the Mach disk, the fluid moves slowly in the core of the jet and it is surrounded by a supersonic moving shell, with a slip line or a shear layer dividing these regions, as shown in Fig. 1.

One of the important parameters describing these supersonic jets is the distance between the vent and the normal shock wave. Experimental results reported in Lewis and Carlson (1964) show that the height of the Mach disk h_d in a pure gas jet depends on the vent diameter D_v , the exit Mach number Ma_v , the ratio of specific heats γ and the ratio K of the exit static pressure P_v and the atmospheric pressure P_{atm} . The empirical relationship is

$$h_d = 0.69 D_v Ma_v \sqrt{\gamma K}. \quad (25)$$

In the case of multiphase gas-particles underexpanded jets, the location of the Mach disk depends also on the particle loading $\eta = \frac{\epsilon_s \rho_s}{\epsilon_g \rho_g}$ at the inlet. Even if in the literature different empirical relationships between Mach disk height and particle loading are proposed (e.g. Lewis and Carlson, 1964; Jarvinen and Draper, 1967; Sommerfeld, 1994), all of them predict an upstream movement of the Mach disk and a reduction of the Mach disk distance from the inlet.

In this section, the aim is to verify if the proposed multiphase model is able to reproduce correctly the wave pattern that forms above an overpressured vent by evaluating the Mach disk location, first in the case of an homogeneous gas, then for a gas-particles mixture.

5.1.1 Homogeneous jet

We consider an homogeneous fluid (dry air with standard chemical components), and we impose underexpanded sonic or supersonic conditions at the inlet (Table 1), i.e. the gas pressure at the inlet is larger than the atmospheric and the Mach number $Ma = |u|/c_s \geq 1$, where c_s is the speed of sound. The computational domain is a box of size $0.1 \times 0.2 \text{ m}^2$, whose left side coincides with the axis of the vent. The side and the

[Title Page](#)[Abstract](#)[Introduction](#)[Conclusions](#)[References](#)[Tables](#)[Figures](#)[◀](#)[▶](#)[◀](#)[▶](#)[Back](#)[Close](#)[Full Screen / Esc](#)[Printer-friendly Version](#)[Interactive Discussion](#)

A numerical model for volcanic jets

S. Carcano et al.

[Title Page](#)[Abstract](#)[Introduction](#)[Conclusions](#)[References](#)[Tables](#)[Figures](#)[◀](#)[▶](#)[◀](#)[▶](#)[Back](#)[Close](#)[Full Screen / Esc](#)[Printer-friendly Version](#)[Interactive Discussion](#)

bottom boundaries of the axisymmetric domain are impermeable and stress free. Two uniform meshes of 160×320 ($\Delta x = \Delta z = 6.25 \times 10^{-4}$ m) and 500×1000 ($\Delta x = \Delta z = 2 \times 10^{-4}$ m) cells have been employed, with time steps of $\Delta t = 10^{-7}$ s and $\Delta t = 5 \times 10^{-8}$ s, respectively. We consider different values of overpressure levels K and we evaluate the height of the Mach disk h_d .

We obtain a good agreement between experimental results and numerical simulations, as shown in Fig. 2. In Figs. 3 and 4, the results obtained in terms of vertical velocity and temperature are shown. The improved version of the PDAC code have a better fit with experimental results and is able to describe the shear layer instability above the Mach disk. In general, the first order version of the model tends to underestimate the Mach disk height. Moreover, for small values of overpressure K , using first order methods we do not see the formation of the Mach disk. Second order methods are able to capture the sharp discontinuity in the flow, as shown in Fig. 5, and allows to obtain a better estimate of the empirical law in Eq. (25).

5.1.2 Non-homogeneous gas-particle jet

When solid particles are added to the gas flow, new phenomena associated to kinetic and thermal non-equilibrium between the gas and particulate phases arise. Such effects are controlled by drag and energy exchange terms in the momentum and energy equations, which are recalled in Appendix A.

To quantify the importance of non-equilibrium regimes, dilute gas-particle flow can be characterized by a time scale (the *particle relaxation time*) determined by the balance between particle inertia and gas-particle viscous drag. Its expression for monodisperse mixtures can be derived from the momentum balance equation for the solid particles (Eq. 5) by neglecting all the terms except the drag and inertial terms:

$$\frac{\partial(\epsilon_s \rho_s w_s)}{\partial t} \simeq D_{g,s}(w_g - w_s), \quad (26)$$

A numerical model
for volcanic jets

S. Carcano et al.

[Title Page](#)[Abstract](#)[Introduction](#)[Conclusions](#)[References](#)[Tables](#)[Figures](#)[◀](#)[▶](#)[◀](#)[▶](#)[Back](#)[Close](#)[Full Screen / Esc](#)[Printer-friendly Version](#)[Interactive Discussion](#)

where we considered only the component along z , since it is much greater than the horizontal components in the decompression region. The relaxation time is thus defined from Eq. (26) as:

$$\tau_s = \frac{\epsilon_s \rho_s}{D_{g,s}}. \quad (27)$$

A simple analysis, e.g. Marble (1970), suggests that the time scale for thermal relaxation has the same order of magnitude.

For dilute mixtures ($\epsilon_g \approx 1$) and low gas-particle Reynolds number, the particle relaxation time approximates that of a single particle in a laminar flow (Stokes' regime):

$$\tau_s \simeq \frac{\rho_s d_s^2}{18 \mu_g}. \quad (28)$$

However, in general, the drag coefficient in Eq. (27) is a complex function of the particle concentration and the gas-particle Reynolds number, which is defined as

$$Re_s = \frac{\epsilon_g \rho_g d_s |\mathbf{v}_g - \mathbf{v}_s|}{\mu_g}. \quad (29)$$

where d_s is the particle diameter and μ_g is the dynamic viscosity of the gas phase. In the underexpanded jet under investigation, the flow is always in a dilute regime, with $\epsilon_g > 0.8$. In these conditions, Eq. (A1) for the drag coefficient (Wen and Yu, 1966) can be adopted and the relaxation time becomes

$$\tau_s \simeq \frac{\epsilon_s \rho_s}{D_{g,s}} = \frac{\epsilon_s \rho_s}{\frac{3}{4} C_{d,s} \frac{\epsilon_g \epsilon_s \rho_g |w_g - w_s|}{d_s} \epsilon_g^{-2.7}} \quad (30)$$

where the coefficient $C_{d,s}$ depends on the gas-particle Reynolds number Re_s , as reported in Eq. (A2).

A numerical model
for volcanic jets

S. Carcano et al.

[Title Page](#)[Abstract](#)[Introduction](#)[Conclusions](#)[References](#)[Tables](#)[Figures](#)[◀](#)[▶](#)[◀](#)[▶](#)[Back](#)[Close](#)[Full Screen / Esc](#)[Printer-friendly Version](#)[Interactive Discussion](#)

The relaxation time τ_s gives an order of magnitude of the time delay with which a particle equilibrates to a time-varying gas flow. In a supersonic jet, such delay may occur in the rapid expansion region above the vent, where a difference between gas and particle velocity Δw may be expected. We should then compare the particle relaxation time with the formation time of the Mach disk (Orescanin et al., 2010), estimated as

$$\tau_{Ma} = \frac{D_v/2}{c_{s,\text{mix}}} \quad (31)$$

where $c_{s,\text{mix}}$ is the mixture speed of sound, as defined e.g. by Pelanti and LeVeque (2006)

$$c_{s,\text{mix}} = \sqrt{\tilde{R}T \frac{\rho_g}{\epsilon_g(\epsilon_g \rho_g + \epsilon_s \rho_s)}} \quad (32)$$

In this section, we consider a mixture of dry air and fine solid particles, with diameter equal to $10\text{ }\mu\text{m}$ and density equal to 2500 kg m^{-3} . Inlet flow parameters correspond to experimental and simulation conditions investigated by Sommerfeld (1994). Gas and particle velocities are both equal to the speed of sound in the pure gas, whereas the overpressure of the gas phase is $K = 31$, producing supersonic underexpanded conditions at the inlet (Table 2). According to the simple scaling analysis discussed above, the ratio between the particle relaxation time and jet time scale is about $\tau_s/\tau_{Ma} > 10^2$. Therefore, we expect that particle will be loosely coupled to the gas phase and that they will not have the time to equilibrate to the expanding gas flow near the vent.

The computational domain is a box of size $0.15 \times 0.225\text{ m}^2$ and, as in the previous test cases, the left side coincides with the axis of the vent, whereas the side and the bottom boundaries of the axisymmetric domain are impermeable and stress free. A non uniform mesh of 500×750 computational cells have been employed, with time step of $\Delta t = 2 \times 10^{-8}\text{ s}$. The maximum resolution is imposed above the inlet, where $\Delta x = \Delta z = 10^{-4}\text{ m}$. We consider different values of particle volume fractions ϵ_s at the inlet and we evaluate the height of the Mach disk h_d .

In Fig. 6 we report the results of four different simulations of particle laden under-expanded jets with different particle concentrations. The gas phase expands radially as in the homogeneous case, thus increasing the final jet radius up to three times in correspondence to the Mach disk location.

On the other hand, as expected from the scaling analysis and also observed in laboratory (Sommerfeld, 1994), particles are almost unaffected by the rapid gas expansion. Particle trajectories remain nearly vertical, with some radial spreading which is almost independent of particle concentration. In the expansion region, particles are only slightly and gradually accelerated by the gas phase (at most by 20 m s^{-1} , up to 368 m s^{-1}) where the Mach disk is located, and then slowly decelerated in the subsonic region, but they never reach an equilibrium condition with the gas phase. However, solid particles tend to deform the Mach disk, moving it towards the vent and making it as more concave as the particle loading increases. For initial particle volume fraction equal to 0.0005, the normal shock is located 14.5 mm from the inlet and the distance is reduced to 12.2 mm when $\epsilon_s = 0.004$. Moreover, increasing the particle loading, the expansion, the acceleration and the cooling of the gas phase are reduced, as shown in Fig. 7. As regards particle distribution, the mixture density profile along the jet axis is not affected by the presence of the shock wave but remains almost constant and displays only a small reduction due to the radial spreading, that tends to increase with increasing particle loading, as observed also by Sommerfeld (1994).

5.2 Pseudogas regime

When particle relaxation time is much lower than the jet time scale, particles are tightly coupled to the gas phase.

Under such assumption, Ogden et al. (2008b) assumed perfect kinematic and thermal equilibrium between the phases and described the eruptive mixture as an homogeneous *pseudogas*, characterized by average thermodynamic and rheologic properties. Two-dimensional numerical simulations of underexpanded volcanic jets were performed with CFDLib, a computational fluid dynamics library developed at Los Alamos

A numerical model for volcanic jets

S. Carcano et al.

[Title Page](#)

[Abstract](#)

[Introduction](#)

[Conclusions](#)

[References](#)

[Tables](#)

[Figures](#)

[◀](#)

[▶](#)

[◀](#)

[▶](#)

[Back](#)

[Close](#)

[Full Screen / Esc](#)

[Printer-friendly Version](#)

[Interactive Discussion](#)



A numerical model for volcanic jets

S. Carcano et al.

[Title Page](#)[Abstract](#)[Introduction](#)[Conclusions](#)[References](#)[Tables](#)[Figures](#)[◀](#)[▶](#)[◀](#)[▶](#)[Back](#)[Close](#)[Full Screen / Esc](#)[Printer-friendly Version](#)[Interactive Discussion](#)

National Laboratory, that uses a finite volume computational scheme with cell-centered state variables. CFDLib applies a variation of the Implicit Continuous-fluid Eulerian (ICE) method, proposed in Harlow and Amsden (1968) and Harlow and Amsden (1975), and a modified Godunov method (Godunov, 1999) to solve shock waves.

Following Ogden et al. (2008b), numerical simulations presented in this section are performed in absence of gravity, in order to focus on compressibility and non-equilibrium multiphase effects. We assume choked flow conditions at the vent, i.e. the inflow velocity is equal to the speed of sound of the mixture, defined by Eq. (32).

Inlet conditions for numerical simulations are specified in Table 3. The mixture is composed by water vapor and solid particles that are injected in a standard atmosphere composed by dry air. We first consider a single solid dispersed phase with particle diameter equal to $10\text{ }\mu\text{m}$. Two different inlet pressure ratios of $K = 20$ (Case A) and $K = 5$ (Case B) were adopted. A third run (Case C) is performed with $K = 5$ and a mixture of two particle phases of $10\text{ }\mu\text{m}$ and $1000\text{ }\mu\text{m}$ equally distributed in weight.

In Case A, the computational domain is a box of size $800 \times 2400\text{ m}^2$ and we use a uniform 200×600 mesh, with $\Delta x = \Delta z = 4\text{ m}$ and a time step $\Delta t = 10^{-4}\text{ s}$. Figure 8 shows the vertical velocity field of the gas phase and the particle distribution above the vent after 20 s, when quasi-steady state conditions are reached. The simulation reproduces the expected behaviour of a supersonic underexpanded jet, displaying the barrel shock with a convex Mach disk, at about 320 m above the vent, which decelerates the mixture down to subsonic velocities (see Fig. 8a) and compresses the gas phase, so that the particle volumetric fraction increases by one order of magnitude across the discontinuity, as shown in Fig. 8b.

To better analyze the jet dynamics and to quantitatively compare our results with those by Ogden et al. (2008b), we study the time-averaged vertical profiles along the axis of pressure, mixture density, gas vertical velocity and gas temperature, shown in Fig. 9. The gas phase undergoes a rapid expansion from the initial pressure of $2.02 \times 10^6\text{ Pa}$ to pressure values below atmospheric pressure. The minimum of the pressure is $9.1 \times 10^3\text{ Pa}$ and it is reached at the height of 324 m above the vent. The

A numerical model
for volcanic jets

S. Carcano et al.

[Title Page](#)[Abstract](#)[Introduction](#)[Conclusions](#)[References](#)[Tables](#)[Figures](#)[◀](#)[▶](#)[◀](#)[▶](#)[Back](#)[Close](#)[Full Screen / Esc](#)[Printer-friendly Version](#)[Interactive Discussion](#)

vertical velocity of the gas phase is 413 ms^{-1} while the minimum temperature along the axis is 1132 K, showing a temperature decrease of about 5 % with respect to the vent temperature.

In Case C, the Mach disk position is unchanged, whereas we observe a peak velocity about 30 ms^{-1} lower. Above the normal shock, gas velocity is 56 ms^{-1} in Case B and 87 ms^{-1} in Case C. Flow density is also considerably higher in Case C. Such differences between Case B and C are associated to the presence of a coarser particulate phase, whose effects are here analyzed in more detail.

5.2.1 Assessment of multiphase effects

10 To assess the influence of non-equilibrium effects on the jet dynamics, we adopt the scaling analysis presented above. To estimate the magnitude of the relaxation time, we first estimate from numerical results the maximum relative Reynolds number, as defined in Eq. (29), in order to estimate the drag coefficient $D_{g,s}$. We consider that the maximum disequilibrium is achieved across the Mach disk, where the gas phase is
15 decelerated almost instantaneously while particles cross the discontinuity undisturbed before slowing down by the effect of viscous drag. By using the gas velocity jump across the shock as a proxy of the velocity difference between the gas and the particles and the gas density after the shock, we estimate the maximum relative gas-particle Reynolds number of the order of 24 (Case A) and 19 (Case B). Therefore, we can use Eq. (28)
20 to estimate the particle relaxation time, obtaining $\tau_s \simeq 1.5 \times 10^{-4} \text{ s}$ (by assuming water vapor viscosity at 1000 K equal to $\mu_g = 3.7 \times 10^{-5} \text{ kg m}^{-1} \text{ s}^{-1}$). We can compare the particle relaxation time with the formation time of the Mach disk defined by Eq. (31).

Taking $T = 1000 \text{ K}$ and considering a dilute mixture of water vapor and solid particle with $\rho_s = 1000 \text{ kg m}^{-3}$, $\epsilon_s = 0.01$, $\rho_g = 0.2 \text{ kg m}^{-3}$, we obtain $c_{s,\text{mix}} \simeq 300 \text{ ms}^{-1}$ and in
25 Case A $\tau_{Ma} \simeq 0.1 \text{ s}$ and in Case B $\tau_{Ma} \simeq 0.03 \text{ s}$. Therefore both in Case A and Case B, the particle relaxation time is much smaller than the formation time of the Mach disk ($\tau_s \ll \tau_{Ma}$), thus meaning that fine particles dynamics are strongly coupled with the

[Title Page](#)[Abstract](#)[Introduction](#)[Conclusions](#)[References](#)[Tables](#)[Figures](#)[◀](#)[▶](#)[◀](#)[▶](#)[Back](#)[Close](#)[Full Screen / Esc](#)[Printer-friendly Version](#)[Interactive Discussion](#)

gas dynamics. Multiphase effects are negligible and the pseudogas approximation is appropriate.

In Case C, we can proceed in an analogous way by assuming that coarse particles move in a fluid composed by water vapor plus fine particles in mechanical and thermal equilibrium, described as a pseudogas (as verified for Cases A and B) and by adopting the same Eqs. (A1) and (A2). We therefore compute the average properties of the pseudogas ρ_{ps} , μ_{ps} and use them to estimate the relaxation time for the coarser particles in a bidisperse mixture.

The particles volume fraction of fine particles decreases by one order of magnitude in the first 10 m above the vent, and further down to 5×10^{-4} before the shock. The pseudogas density before the shock is $\rho_{ps} = \epsilon_g \rho_g + \epsilon_{s_1} \rho_{s_1} = 1.2 \text{ kg m}^{-3}$. Its mean viscosity can be computed as $\mu_{ps} \simeq \mu_g (1 + 2.5 \epsilon_{s_1}) = 3.71 \times 10^{-5} \text{ Pas}$ (Einstein, 1906), not very different from the value for pure water vapor. The maximum gas-particles Reynolds number, computed from the gas velocity jump across the shock $|w_g^b - w_g^a| = 298 \text{ ms}^{-1}$, is $Re_s \simeq 9 \times 10^3$, thus implying that the low- Re approximation in Eq. (28) for the relaxation time is not applicable. In regimes where $Re_s > 1000$ we can estimate the relaxation time with the Reynolds number correction, as reported in Eq. (A2), that is

$$\tau_s \simeq \frac{\epsilon_{s_2} \rho_s}{D_{ps,s_2}} = \frac{\rho_{s_2} d_{s_2}^2}{0.33 Re_{s_2} \mu_{ps}} \simeq 0.01 \text{ s.} \quad (33)$$

In Case C the particle relaxation time and the formation time of the Mach disk are comparable, thus it is worth investigating in detail the non-equilibrium effects for the coarsest particles.

We first estimate the magnitude of the velocity difference between gas and particle below the shock as $\Delta w^{\text{est}} \approx \alpha \tau_s w_g^b$, where $\alpha = \frac{dw_g}{dz}$ is the gas velocity vertical gradient below the shock, and w_g^b is the gas vertical velocity below the shock, as computed in the equilibrium gas-particle flow. Based on the results discussed in the previous section (see Figs. 9 and 11) α is taken as constant. In the expansion region, the velocity

[Title Page](#)

[Abstract](#)

[Introduction](#)

[Conclusions](#)

[References](#)

[Tables](#)

[Figures](#)

[◀](#)

[▶](#)

[◀](#)

[▶](#)

[Back](#)

[Close](#)

[Full Screen / Esc](#)

[Printer-friendly Version](#)

[Interactive Discussion](#)



gradient α is approximatively equal to 6 s^{-1} , the gas velocity is $w_g^b = 386\text{ ms}^{-1}$, and we obtain $\Delta w_C^{\text{est}} \simeq 23\text{ ms}^{-1}$.

Across the normal shock, on the other hand, particles will equilibrate to the gas flow within a distance l , also known as shock relaxation (Marble, 1970). We can derive an estimate of the relaxation distance above the shock as $l^{\text{est}} = |w_g^b - w_g^a| \cdot \tau_s$, where $|w_g^b - w_g^a|$ is the gas velocity jump across the normal shock. Across the Mach disk, the jump in vertical gas velocity is 299 ms^{-1} . The distance to which particles equilibrate to the gas flow above the shock can be computed by assuming an initial disequilibrium velocity of the same order of magnitude and the relaxation time, obtaining $l_C^{\text{est}} \simeq |w_g^b - w_g^a| \cdot \tau_s \simeq 3\text{ m}$.

Figure 12 shows the differences between gas and particles velocity and temperature in Case C as they result from the numerical code. We observe that smaller particles are essentially in thermal and mechanical equilibrium with the gas phase, as expected from theoretical results. Larger particles just below the normal shock are slower than the gas of about 25 ms^{-1} , they cross the shock with a vertical velocity that is about 140 ms^{-1} larger than the gas vertical velocity and finally they reach an equilibrium velocity close to the gas velocity. Larger particles tends to cool slower than the gas and the smaller particles and so their temperature is about 70 K higher than the gas temperature when they reach the Mach disk. The estimated relaxation length is larger than the vertical grid size (0.4 m), so that numerical resolution appear adequate to quantitatively resolve shock relaxation. In particular, after the normal shock, particles slow down to the gas velocity within 6 computational cells, from 40.4 m to 42.8 m . The numerical estimate of the relaxation distance $l_C \simeq 2.4\text{ m}$ is thus comparable with the theoretical one $l_C^{\text{est}} \simeq 3\text{ m}$.

Numerical results are therefore consistent with estimates derived from pseudogas solution and a simple dimensional analysis based on the particle relaxation time.

[Title Page](#)[Abstract](#)[Introduction](#)[Conclusions](#)[References](#)[Tables](#)[Figures](#)[◀](#)[▶](#)[◀](#)[▶](#)[Back](#)[Close](#)[Full Screen / Esc](#)[Printer-friendly Version](#)[Interactive Discussion](#)

5.3 Three-dimensional simulations

We repeated some of the simulations presented in the previous sections in a three-dimensional configuration, in order to compare the results with those obtained in the two-dimensional axisymmetric tests. In this section, we present the results obtained

5 with the vent conditions of Case B (see Table 2). The computational domain is a box of size $400 \times 400 \times 400 \text{ m}^3$, we use a non-uniform mesh of $120 \times 120 \times 120$ cells and a time step $\Delta t = 10^{-4} \text{ s}$, with maximum grid resolution of 1 m (equal to that employed in 2-D) in a subdomain of $50 \times 50 \times 50 \text{ m}^3$ above the vent. Figure 13 shows the isosurfaces of the gas vertical velocity at $t = 2 \text{ s}$. Figure 14 shows the 3-D vertical velocity and
10 the logarithm to the base 10 of total particle volumetric fraction averaged along the azimuthal angle. With respect to the 2-D simulation in cylindrical symmetry (Fig. 10), 3-D simulation displays a more diffused jet boundary likely associated to the effect of the non-circular inlet. Indeed, with Cartesian mesh discretization, the circular vent is approximated by squared cells. The flow density have been opportunely corrected in
15 cells cut by the inlet rim by proportionally reducing the particle concentration, in order to impose the correct mass flow rate. However, boundary conditions do not describe the curved inlet rim. This produces some axial switching of the jet cross section in the subsonic region above the Mach disk, analogous to that observed in non-circular subsonic jets (e.g. Gutmark and Grinstein, 1999).

20 Nonetheless, the shock wave pattern (location and shape of the Mach disk and slip lines) is analogous to the 2-D case. Figure 15 shows that the time-averaged axial profiles of pressure, velocity, mixture density are consistent with the results obtained with two dimensional axisymmetric simulations. Temperature difference probably reflects some differences in the average axial distribution of solid particles associated to the
25 approximate vent geometry.

A numerical model for volcanic jets

S. Carcano et al.

[Title Page](#)

[Abstract](#)

[Introduction](#)

[Conclusions](#)

[References](#)

[Tables](#)

[Figures](#)

◀

▶

◀

▶

[Back](#)

[Close](#)

[Full Screen / Esc](#)

[Printer-friendly Version](#)

[Interactive Discussion](#)



6 Conclusions

The PDAC multiphase flow model has been improved in several aspects of the numerical algorithm to improve the temporal and spatial accuracy of the simulation of explosive volcanic eruptions. In the new model version, a second order Crank–Nicolson type time discretization has been introduced and the fully multidimensional advection schemes proposed by LeVeque (1996) have been employed. The new model has been tested against the complex problem of volcanic jet decompression in both two and three dimensions. Since a proper validation with volcanic jet data is not yet possible, due to the large scale and dangerous nature of the phenomenon and the difficulty of remote measurements, we have verified that the numerical results adequately reproduce some similar phenomenology (i.e. an underexpanded, supersonic gas jet) in the laboratory, where the new numerical scheme demonstrates a better performance (in terms of accuracy and reduced numerical diffusion) with respect to previous model versions at all regimes.

However, several aspects of the dynamics of volcanic jets make them different from their laboratory analogous: volcanic jets involve the explosive decompression of a multiphase gas-particle mixture at high temperature, with a wide spectrum of particle grain sizes. To account for the presence of solid particles in supersonic volcanic jets, previous workers have described the eruptive mixture as an homogeneous pseudogas (e.g. Kieffer, 1984; Woods and Bower, 1995; Ogden et al., 2008b; Orescanin et al., 2010). In the limiting case of fine particles (having diameter of the order of 10 microns and relaxation time of the order of 10^{-4} s, much smaller than the characteristic time for decompression), we have shown that the multiphase PDAC model consistently reproduce predictions of the pseudogas model. However, in the case of coarse particles and polydisperse mixtures, multiphase effects become more important and also affect the average jet dynamics.

The new numerical code appears therefore suited for the multiphase flow simulation of explosive regimes characterized by rapid decompression of the eruptive mixture

A numerical model for volcanic jets

S. Carcano et al.

[Title Page](#)

[Abstract](#)

[Introduction](#)

[Conclusions](#)

[References](#)

[Tables](#)

[Figures](#)

[◀](#)

[▶](#)

[◀](#)

[▶](#)

[Back](#)

[Close](#)

[Full Screen / Esc](#)

[Printer-friendly Version](#)

[Interactive Discussion](#)



[Title Page](#)[Abstract](#)[Introduction](#)[Conclusions](#)[References](#)[Tables](#)[Figures](#)[◀](#)[▶](#)[◀](#)[▶](#)[Back](#)[Close](#)[Full Screen / Esc](#)[Printer-friendly Version](#)[Interactive Discussion](#)

and possible transition to supersonic regime, including the development of impulsive Vulcanian eruptions and volcanic blasts, which will be addressed in future works. In this context, multiphase effects will be quantified also for polydisperse mixtures, where particle-particle drag might play a key role in the non-equilibrium dynamics of gas-particle flows.

Appendix A

Gas-particle non-equilibrium coefficients

The drag coefficient between gas and solid particles is a complex function of the particle concentration and the gas-particle Reynolds number defined in Eq. (29). In the dilute regime $\epsilon_g \geq 0.8$, we adopt the drag expression proposed by Wen and Yu (1966):

$$D_{g,s} = D_{s,g} = \frac{3}{4} C_{d,s} \frac{\epsilon_g \epsilon_s \rho_g |\mathbf{v}_g - \mathbf{v}_s|}{d_s} \epsilon_g^{-2.7}, \quad (A1)$$

for all $s = 1 \dots N$, with

$$C_{d,s} = \begin{cases} \frac{24}{Re_s} \left[1 + 0.15 Re_s^{0.687} \right], & \text{if } Re_s < 1000, \\ 0.44, & \text{if } Re_s \geq 1000 \end{cases} \quad (A2)$$

In the dense regime $\epsilon_g < 0.8$, we adopt the drag expression proposed in Ergun (1952):

$$D_{g,s} = 150 \frac{\epsilon_s^2 \mu_g}{\epsilon_g d_s^2} + 1.75 \frac{\epsilon_s \rho_g |\mathbf{v}_g - \mathbf{v}_s|}{d_s}, \quad s = 1, \dots, N \quad (A3)$$

The heat transfer between the gas and the solid phases is given by the product of a transfer coefficient Q_s and a driving force, which is the difference in temperature

between the two phases. The coefficient Q_s represents the volumetric interphase heat transfer coefficient, which equals the product of the specific exchange area and the fluid-particle heat transfer coefficient.

$$_5 \quad Q_s = 6Nu_s k_g \epsilon_s / d_s \quad (A4)$$

where the empirical expression for the Nusselt number Nu_s is taken as:

$$Nu_s = (2 + 5\epsilon_s^2) (1 + 0.7Re_s^{0.2}Pr^{1/3}) + (0.13 + 1.2\epsilon_s^2 Re_s^{0.7}Pr^{1/3}), \quad (A5)$$

(Gunn, 1978), for $Re_s \leq 10^5$

$$_{10} \quad Re_s = \frac{\rho_g d_s |\mathbf{v}_g - \mathbf{v}_s|}{\mu_s}, \quad Pr = \frac{c_{p,g} \mu_g}{k_g}, \quad (A6)$$

and k_g is the thermal conductivity of the gas phase.

[Title Page](#)[Abstract](#)[Introduction](#)[Conclusions](#)[References](#)[Tables](#)[Figures](#)[◀](#)[▶](#)[◀](#)[▶](#)[Back](#)[Close](#)[Full Screen / Esc](#)[Printer-friendly Version](#)[Interactive Discussion](#)

Explicit terms in discretized equations

The expressions of the discrete explicit terms of the momentum equations of the gas and the solid phase are the following:

$$5 \quad \begin{aligned} \mathcal{E}_{u_s, i+\frac{1}{2}jk}^n &= (\bar{\epsilon}_s \bar{\rho}_s u_s)_{i+\frac{1}{2}jk}^n - (1 - \theta) \frac{\Delta t}{\Delta x} \bar{\epsilon}_{s, i+\frac{1}{2}jk}^n (p_{g, i+1jk}^n - p_{g, ijk}^n) \\ &+ (1 - \theta) \Delta t D_{ps, i+\frac{1}{2}jk}^n (u_{p, i+\frac{1}{2}jk}^n - u_{s, i+\frac{1}{2}jk}^{n+1}) + (1 - \theta) \Delta t (\bar{\epsilon}_s \bar{\rho}_s g_x)_{i+\frac{1}{2}jk}^n \\ &- \frac{\Delta t}{\Delta x} \langle \bar{\epsilon}_s \bar{\rho}_s u_s^2 \rangle_{i+\frac{1}{2}jk}^n - \frac{\Delta t}{\Delta y} \langle \bar{\epsilon}_s \bar{\rho}_s u_s \bar{v}_s \rangle_{i+\frac{1}{2}jk}^n - \frac{\Delta t}{\Delta z} \langle \bar{\epsilon}_s \bar{\rho}_s u_s \bar{w}_s \rangle_{i+\frac{1}{2}jk}^n, \end{aligned} \quad (B1)$$

$$\begin{aligned} \mathcal{E}_{v_s, ij+\frac{1}{2}k}^n &= (\bar{\epsilon}_s \bar{\rho}_s v_s)_{ij+\frac{1}{2}k}^n - (1 - \theta) \frac{\Delta t}{\Delta y} \bar{\epsilon}_{s, ij+\frac{1}{2}k}^n (p_{g, ij+1k}^n - p_{g, ijk}^n) \\ &+ (1 - \theta) \Delta t D_{ps, ij+\frac{1}{2}k}^n (v_{p, ij+\frac{1}{2}k}^n - v_{s, ij+\frac{1}{2}k}^n) + (1 - \theta) \Delta t (\bar{\epsilon}_s \bar{\rho}_s g_y)_{ij+\frac{1}{2}k}^n \\ &- \frac{\Delta t}{\Delta x} \langle \bar{\epsilon}_s \bar{\rho}_s v_s \bar{u}_s \rangle_{ij+\frac{1}{2}k}^n - \frac{\Delta t}{\Delta y} \langle \bar{\epsilon}_s \bar{\rho}_s v_s^2 \rangle_{ij+\frac{1}{2}k}^n - \frac{\Delta t}{\Delta z} \langle \bar{\epsilon}_s \bar{\rho}_s v_s \bar{w}_s \rangle_{ij+\frac{1}{2}k}^n, \end{aligned} \quad (B2)$$

$$\begin{aligned} \mathcal{E}_{w_s, ijk+\frac{1}{2}}^n &= (\bar{\epsilon}_s \bar{\rho}_s w_s)_{ijk+\frac{1}{2}}^n - (1 - \theta) \frac{\Delta t}{\Delta z} \bar{\epsilon}_{s, ijk+\frac{1}{2}}^n (p_{g, ijk+1}^n - p_{g, ijk}^n) \\ &+ (1 - \theta) \Delta t D_{ps, ijk+\frac{1}{2}}^n (w_{p, ijk+\frac{1}{2}}^n - w_{s, ijk+\frac{1}{2}}^n) + (1 - \theta) \Delta t (\bar{\epsilon}_s \bar{\rho}_s g_z)_{ijk+\frac{1}{2}}^n \\ &- \frac{\Delta t}{\Delta x} \langle \bar{\epsilon}_s \bar{\rho}_s w_s \bar{u}_s \rangle_{ijk+\frac{1}{2}}^n - \frac{\Delta t}{\Delta y} \langle \bar{\epsilon}_s \bar{\rho}_s w_s \bar{v}_s \rangle_{ijk+\frac{1}{2}}^n - \frac{\Delta t}{\Delta z} \langle \bar{\epsilon}_s \bar{\rho}_s w_s^2 \rangle_{ijk+\frac{1}{2}}^n. \end{aligned} \quad (B3)$$

[Title Page](#)

[Abstract](#)

[Introduction](#)

[Conclusions](#)

[References](#)

[Tables](#)

[Figures](#)

◀

▶

◀

▶

[Back](#)

[Close](#)

[Full Screen / Esc](#)

[Printer-friendly Version](#)

[Interactive Discussion](#)



The expressions of the discrete explicit terms of the energy equations of the gas and the solid phase are the following:

$$\begin{aligned} \mathcal{E}_{h_g,ijk}^n = & (\epsilon_g \rho_g h_g)_{ijk}^n + (1 - \theta) \Delta t Q_{s,ijk}^n (T_s - T_g)_{ijk}^n \\ & - \frac{\Delta t}{\Delta x} \langle \epsilon_g \rho_g h_g^n \bar{u}_g \rangle_{ijk}^{n+1} - \frac{\Delta t}{\Delta y} \langle \epsilon_g \rho_g h_g^n \bar{v}_g \rangle_{ijk}^{n+1} - \frac{\Delta t}{\Delta z} \langle \epsilon_g \rho_g h_g^n \bar{w}_g \rangle_{ijk}^{n+1} \\ & + \epsilon_{g,ijk}^{n+1} (p_{g,ijk}^{n+1} - p_{g,ijk}^n) + \frac{\Delta t}{\Delta x} (\bar{u}_g \epsilon_g)_{ijk}^{n+1} (\bar{p}_{g,i+\frac{1}{2}jk}^{n+1} - \bar{p}_{g,i-\frac{1}{2}jk}^{n+1}) \\ & + \frac{\Delta t}{\Delta y} (\bar{v}_g \epsilon_g)_{ijk}^{n+1} (\bar{p}_{g,j+\frac{1}{2}k}^{n+1} - \bar{p}_{g,j-\frac{1}{2}k}^{n+1}) + \frac{\Delta t}{\Delta z} (\bar{w}_g \epsilon_g)_{ijk}^{n+1} (\bar{p}_{g,ijk+\frac{1}{2}}^{n+1} - \bar{p}_{g,ijk-\frac{1}{2}}^{n+1}), \end{aligned} \quad (B4)$$

$$\begin{aligned} \mathcal{E}_{h_s,ijk}^n = & (\epsilon_s \rho_s h_s)_{ijk}^n + (1 - \theta) \Delta t Q_{s,ijk}^n (T_g - T_s)_{ijk}^n \\ & - \frac{\Delta t}{\Delta x} \langle \epsilon_s \rho_s h_s^n \bar{u}_s \rangle_{ijk}^{n+1} - \frac{\Delta t}{\Delta y} \langle \epsilon_s \rho_s h_s^n \bar{v}_s \rangle_{ijk}^{n+1} - \frac{\Delta t}{\Delta z} \langle \epsilon_s \rho_s h_s^n \bar{w}_s \rangle_{ijk}^{n+1}. \end{aligned} \quad (B5)$$

Acknowledgements. This work presents intermediate results achieved in the PhD thesis work of the first named author (S.C.), carried out at MOX – Politecnico di Milano and Istituto Nazionale di Geofisica e Vulcanologia, Sezione di Pisa. Financial support from Dipartimento della Protezione Civile (Italy) through the SPEED and V1 projects is acknowledged. Useful discussions with L. Formaggia, E. Miglio and F. Nobile are gratefully acknowledged. We also acknowledge the CINECA Award N. HP10C9QQCS, 2011 for the availability of high performance computing resources and support.

References

Arakawa, A. and Lamb, V. R.: A potential enstrophy and energy conserving scheme for the shallow water equations., *Mon. Weather Rev.*, 109, 18–36, 1981. 411

Carcano, S., Bonaventura, L., Neri, A., and Esposti Ongaro, T.: A second order accurate numerical model for multiphase underexpanded volcanic jets, *MOX Report 50/2012*, MOX – Politecnico di Milano, Milano, 2012. 405, 412

Colella, P.: Multidimensional upwind methods for hyperbolic conservation laws, *J. Comput. Phys.*, 87, 171–200, 1990. 412, 413

Crank, J. and Nicolson, P.: A practical method for numerical evaluation of solutions of partial differential equations of the heat-conduction type, *P. Camb. Philos. Soc.*, 43, 50–67, 1947. 403, 408

[Title Page](#)

[Abstract](#)

[Introduction](#)

[Conclusions](#)

[References](#)

[Tables](#)

[Figures](#)

◀

▶

◀

▶

[Back](#)

[Close](#)

[Full Screen / Esc](#)

[Printer-friendly Version](#)

[Interactive Discussion](#)



A numerical model for volcanic jets

S. Carcano et al.

[Title Page](#)[Abstract](#)[Introduction](#)[Conclusions](#)[References](#)[Tables](#)[Figures](#)[◀](#)[▶](#)[◀](#)[▶](#)[Back](#)[Close](#)[Full Screen / Esc](#)[Printer-friendly Version](#)[Interactive Discussion](#)

A numerical model for volcanic jets

S. Carcano et al.

[Title Page](#)[Abstract](#)[Introduction](#)[Conclusions](#)[References](#)[Tables](#)[Figures](#)[◀](#)[▶](#)[◀](#)[▶](#)[Back](#)[Close](#)[Full Screen / Esc](#)[Printer-friendly Version](#)[Interactive Discussion](#)

A numerical model
for volcanic jets

S. Carcano et al.

[Title Page](#)[Abstract](#)[Introduction](#)[Conclusions](#)[References](#)[Tables](#)[Figures](#)[◀](#)[▶](#)[◀](#)[▶](#)[Back](#)[Close](#)[Full Screen / Esc](#)[Printer-friendly Version](#)[Interactive Discussion](#)

Oreskes, N., Shrader-Frechette, K., and Belitz, K.: Verification, validation, and confirmation of numerical models in the Earth Sciences, *Science*, 263, 641–646, 1994. 403

Parfitt, E. A. and Wilson, L.: *Fundamentals of Physical Volcanology*, Blackwell Publishing, Malden, USA, 2008. 401

5 Pelanti, M. and LeVeque, R. J.: High-resolution finite volume methods for dusty gas jets and plumes, *SIAM J. Sci. Comput.*, 28, 1335–1360, 2006. 402, 418

Quarteroni, A., Sacco, R., and Saleri, F.: *Numerical Mathematics*, Springer-Verlag, Berlin, 2002. 408

10 Roe, P. L.: Characteristic-based schemes for the Euler equations, *Annu. Rev. Fluid Mech.*, 18, 337–365, 1986. 413

Saltzman, J.: An unsplit 3D upwind method for hyperbolic conservation laws, *J. Comput. Phys.*, 115, 153–168, 1993. 413

Sommerfeld, M.: The structure of particle-laden, underexpanded free jets, *Shock Waves*, 3, 299–311, 1994. 415, 418, 419

15 Sparks, R. S. J., Bursik, M. I., Carey, S. N., Gilbert, J. S., Glaze, L. S., Sigurdsson, H., and Woods, A. W.: *Volcanic Plumes*, John Wiley, New York, 1997. 401

Suzuki, Y. J. and Koyaguchi, T.: Numerical determination of the efficiency of entrainment in volcanic eruption columns, *Geophys. Res. Lett.*, 37(5), L05302, doi:10.1029/2009GL042159, 2010. 402

20 Suzuki, Y. J., Koyaguchi, T., Ogawa, M., and Hachisu, I.: A numerical study of turbulent mixing in eruption clouds using a three-dimensional fluid dynamics model, *J. Geophys. Res.*, 110(8), B08201, doi:10.1029/2004JB003460, 2005. 401

Sweby, P.: High resolution schemes using flux-limiters for hyperbolic conservation laws, *SIAM J. Numer. Anal.*, 21, 995–1011, 1984. 402

25 Syamlal, M.: MFIX documentation: numerical technique, Tech. rep., U.S. Department of energy, Office of fossil energy, Federal Energy Technology Center, Morgantown, West Virginia, USA, 1998. 402

Syamlal, M., Rogers, W., and O'Brien, T. J.: MFIX documentation: technical note, Tech. rep., U.S. Department of energy, Office of fossil energy, Morgantown Energy Technology Center, Morgantown, West Virginia, USA, 1993. 402

30 Valentine, G. A.: *Eruption column physics*, vol. 4, pp. 91–138, A. Freud and M. Rosi, Elsevier, Netherlands, 1998. 401

Valentine, G. A. and Wohletz, K. H.: Numerical models of Plinian eruption columns and pyroclastic flows, *J. Geophys. Res.*, 94(B2), 1867–1887, 1989. 402

Wen, C. Y. and Yu, Y. H.: Mechanics of fluidization, *Chem. Eng. Prog. S. Ser.*, 62, 100–111, 1966. 417, 427

5 Wilson, L.: Explosive volcanic eruptions – III – Plinian eruption columns, *Geophys. J. Roy. Astr. S.*, 45, 543–556, 1976. 401

Woods, A. W.: The dynamics and thermodynamics of eruption columns, *B. Volcanol.*, 50, 169–193, 1988. 401

Woods, A. W. and Bower, S. M.: The decompression of volcanic jets in a crater during explosive volcanic eruptions, *Earth Planet. Sc. Lett.*, 131, 189–205, 1995. 401, 426

10

A numerical model for volcanic jets

S. Carcano et al.

[Title Page](#)[Abstract](#)[Introduction](#)[Conclusions](#)[References](#)[Tables](#)[Figures](#)[|◀](#)[▶|](#)[◀](#)[▶](#)[Back](#)[Close](#)[Full Screen / Esc](#)[Printer-friendly Version](#)[Interactive Discussion](#)

A numerical model for volcanic jets

S. Carcano et al.

Title Page

Abstract

Introduction

Conclusion

Reference

Table

Figure

Back

Close

Full Screen / Esc

[Printer-friendly Version](#)

Interactive Discussion



Table 1. Inlet conditions for a homogeneous underexpanded jet at the laboratory scale.

D_v	[m]	0.01
$K = p_v/p_{atm}$		2, 5, 10, 20
w_v	[$m s^{-1}$]	346
T_v	[K]	298
Ma_v		1.0

**A numerical model
for volcanic jets**

S. Carcano et al.

Table 2. Inlet conditions for a inhomogeneous underexpanded jet at the laboratory scale.

D_v	[m]	0.003
K		31
w	[ms^{-1}]	347
T	[K]	300
ϵ_s		0.0005, 0.001, 0.002, 0.004
d_s	[μm]	10
ρ_s	[kg m^{-3}]	2500

[Title Page](#)[Abstract](#)[Introduction](#)[Conclusions](#)[References](#)[Tables](#)[Figures](#)[◀](#)[▶](#)[◀](#)[▶](#)[Back](#)[Close](#)[Full Screen / Esc](#)[Printer-friendly Version](#)[Interactive Discussion](#)

Table 3. Inlet conditions of the inhomogeneous underexpanded jets.

		Case A	Case B	Case C
D_v	[m]	80	20	20
K		20	5	5
w	[m s^{-1}]	150.3	150.3	150.3
T	[K]	1200	1200	1200
Ma_v		1.0	1.0	1.0
ϵ_{s_1}		0.08784	0.021985	0.010992
d_{s_1}	[μm]	10	10	10
ρ_{s_1}	[kg m^{-3}]	1000	1000	1000
ϵ_{s_2}		–	–	0.010992
d_{s_2}	[μm]	–	–	1000
ρ_{s_2}	[kg m^{-3}]	–	–	1000

[Title Page](#)[Abstract](#)[Introduction](#)[Conclusions](#)[References](#)[Tables](#)[Figures](#)[◀](#)[▶](#)[◀](#)[▶](#)[Back](#)[Close](#)[Full Screen / Esc](#)[Printer-friendly Version](#)[Interactive Discussion](#)

**A numerical model
for volcanic jets**

S. Carcano et al.

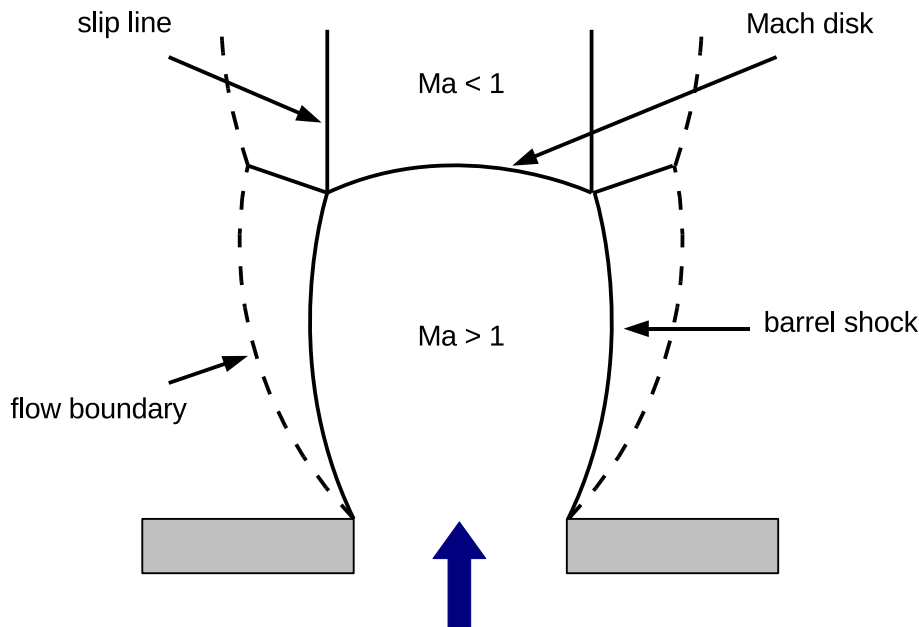


Fig. 1. Decompression structure in underexpanded supersonic jets.

[Title Page](#)[Abstract](#)[Introduction](#)[Conclusions](#)[References](#)[Tables](#)[Figures](#)[◀](#)[▶](#)[◀](#)[▶](#)[Back](#)[Close](#)[Full Screen / Esc](#)[Printer-friendly Version](#)[Interactive Discussion](#)

A numerical model for volcanic jets

S. Carcano et al.

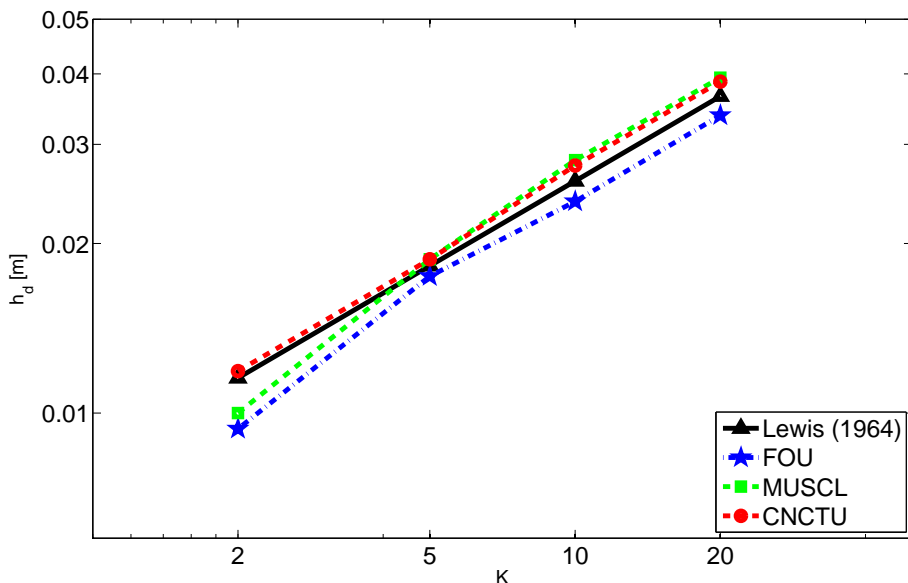


Fig. 2. Comparison between experimental and numerical results in terms of Mach disk height for different values of the vent overpressure K . The results in Lewis and Carlson (1964) are compared with numerical simulation applying first order donor-cell upwind method (FOU), upwind method with second order MUSCL fluxes (MUSCL) and second order Corner Transport Upwind method with θ -method time discretization (CNCTU).

Title Page

Abstract

Introduction

Conclusion

References

Table

Figures

1

1

Bar

Close

Full Screen / Esc

Interactive Discussion



A numerical model for volcanic jets

S. Carcano et al.

Title Page

Abstract

Introduction

Conclusi

References

Tables

Figures

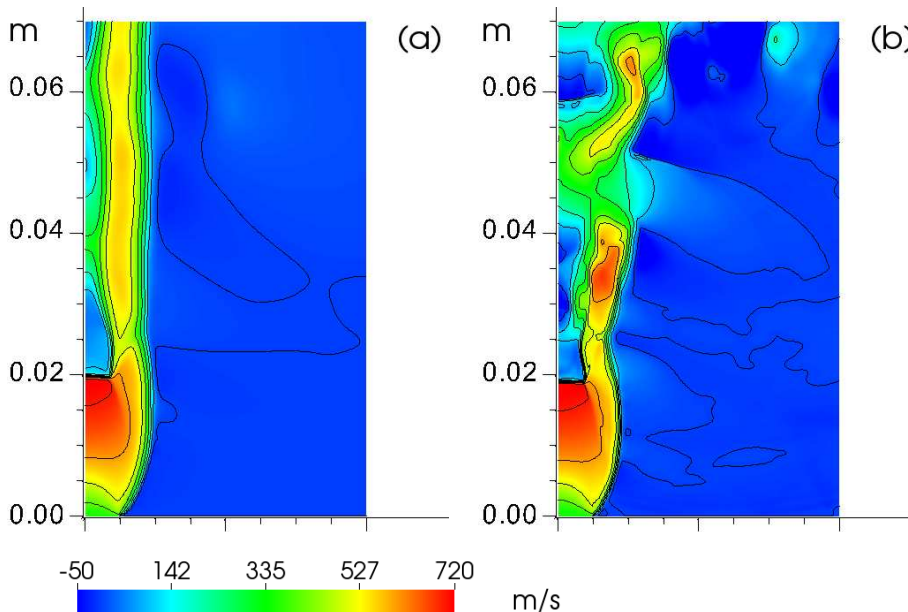
1

Back

Close

Full Screen / Esc

Fig. 3. Vertical velocity at $t = 10^{-3}$ s. Isolines $[0 : 100 : 700] \text{ ms}^{-1}$. Comparison between **(a)** first order upwind method FOU and **(b)** second order method CNCTU with $K = 5$ on a 500×1000 mesh.



A numerical model for volcanic jets

S. Carcano et al.

Title Page

Abstract

Introduction

Conclusion

References

Table

Figures

1

Bac

Close

Full Screen / Esc

[Printer-friendly Version](#)

Interactive Discussion

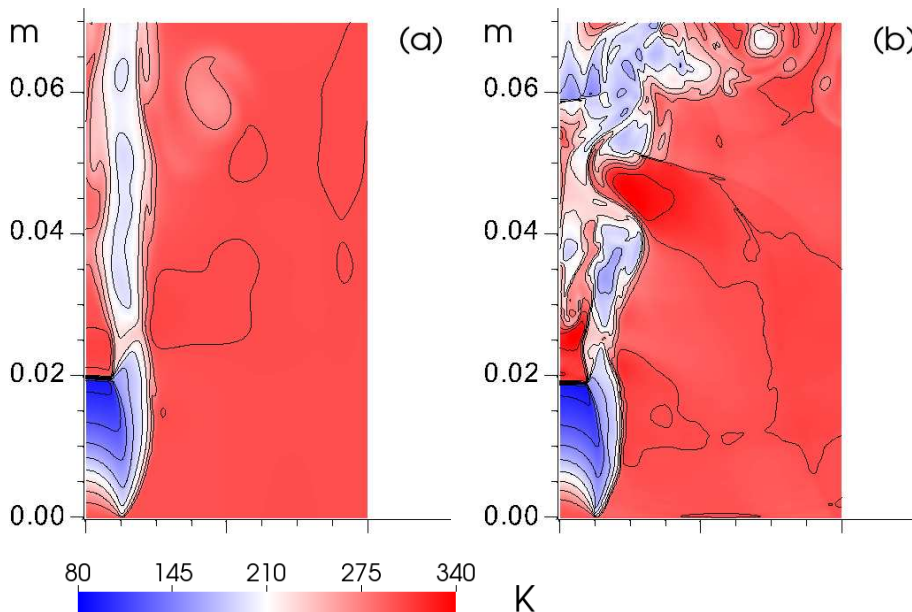


Fig. 4. Temperature at $t = 10^{-3}$ s. Isolines [50 : 25 : 350] K. Comparison between **(a)** first order upwind method FOU and **(b)** second order method CNCTU with $K = 5$ on a 500×1000 mesh.

A numerical model for volcanic jets

S. Carcano et al.

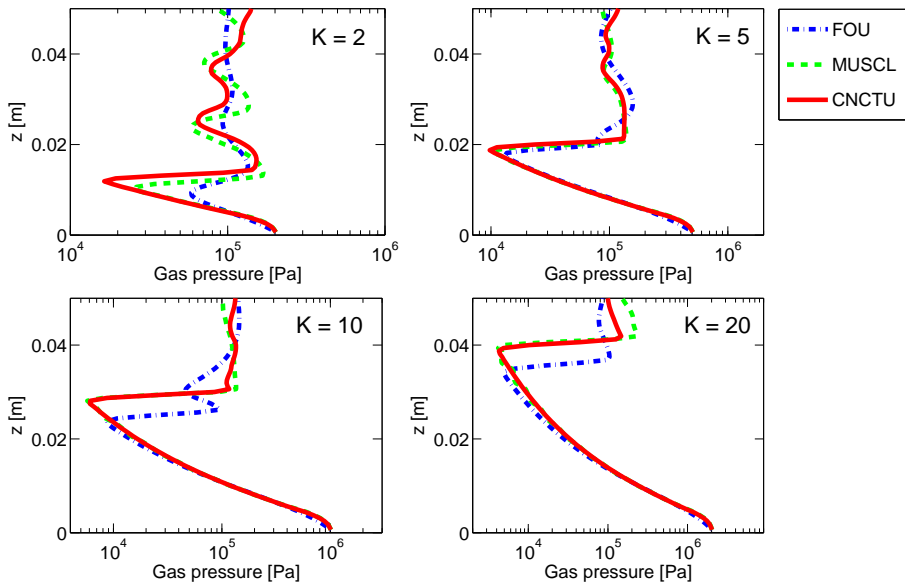


Fig. 5. Gas pressure at $t = 2 \times 10^{-3}$ s. Axial profile for different values of the vent overpressure K computed on a coarse mesh. Comparison between first order (FOU) and second order methods (MUSCL and CNCTU) on a 160×320 mesh.

[Title Page](#)

[Abstract](#)

[Introduction](#)

[Conclusions](#)

[References](#)

[Tables](#)

[Figures](#)

◀

▶

◀

▶

[Back](#)

[Close](#)

[Full Screen / Esc](#)

[Printer-friendly Version](#)

[Interactive Discussion](#)

A numerical model
for volcanic jets

S. Carcano et al.

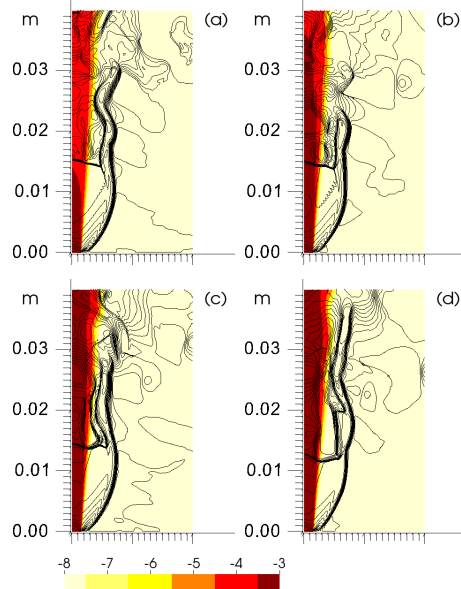


Fig. 6. Isolines [0 : 50 : 700] m s^{-1} of gas vertical velocity and logarithm to the base 10 of particle volume fraction at $t = 3 \times 10^{-4}$ s for different values of initial particle volume fraction **(a)** $\epsilon_s = 0.0005$, **(b)** $\epsilon_s = 0.001$, **(c)** $\epsilon_s = 0.002$, **(d)** $\epsilon_s = 0.004$.

A numerical model for volcanic jets

S. Carcano et al.

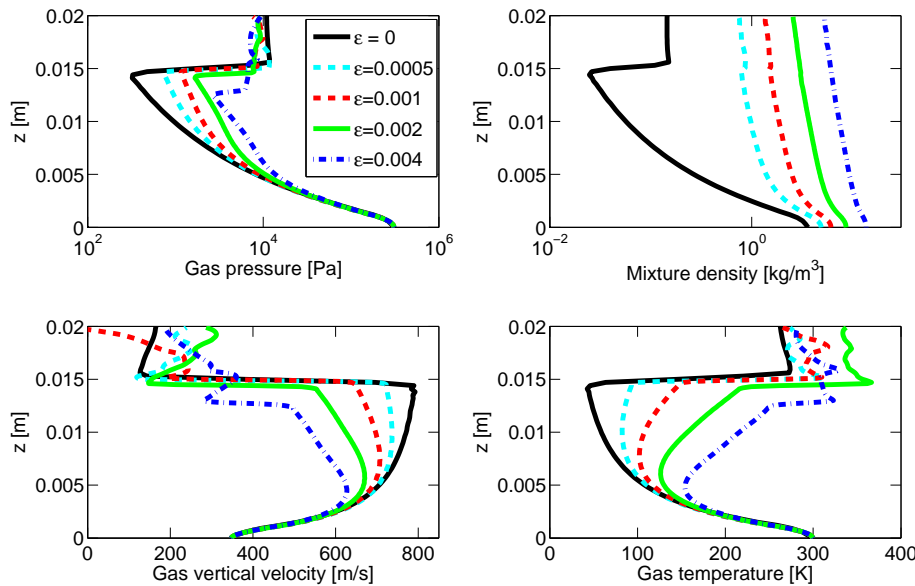


Fig. 7. Axial profile of gas pressure, mixture density, gas vertical velocity and gas temperature at $t = 3 \times 10^{-4}$ s. Comparison between homogeneous jet's profile and results obtained for different values of initial particle volume fraction $\epsilon_s = 0.0005, 0.001, 0.002, 0.004$.

[Title Page](#)

[Abstract](#)

[Introduction](#)

[Conclusions](#)

[References](#)

[Tables](#)

[Figures](#)

◀

▶

◀

▶

[Back](#)

[Close](#)

[Full Screen / Esc](#)

[Printer-friendly Version](#)

[Interactive Discussion](#)

**A numerical model
for volcanic jets**

S. Carcano et al.

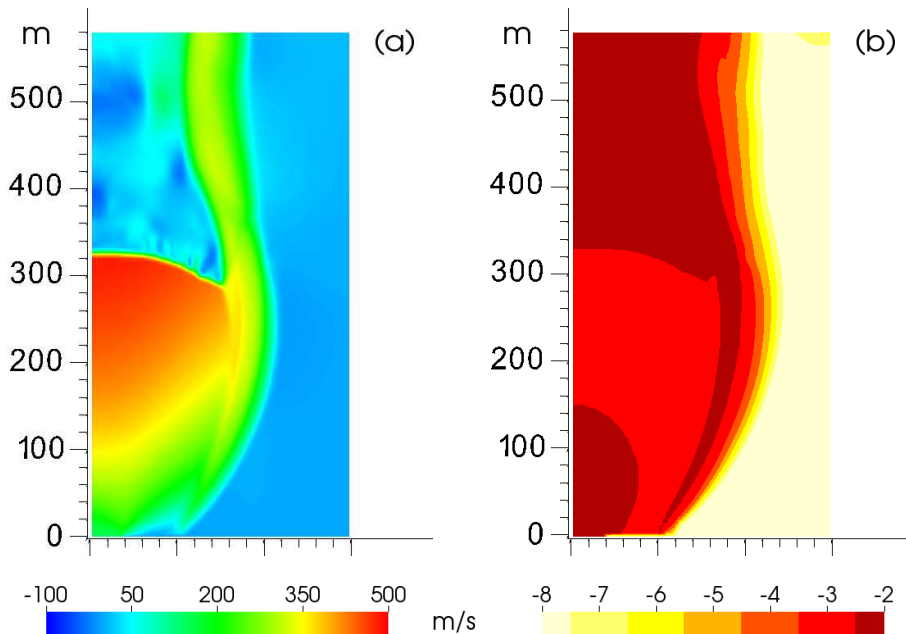


Fig. 8. Case A. **(a)** Gas vertical velocity [m s^{-1}] and **(b)** logarithm to the base 10 of particle volume fraction. Snapshots at $t = 20 \text{ s}$.

[Title Page](#) [Abstract](#) [Introduction](#)
[Conclusions](#) [References](#)
[Tables](#) [Figures](#)
[◀](#) [▶](#)
[◀](#) [▶](#)
[Back](#) [Close](#)
[Full Screen / Esc](#)

[Printer-friendly Version](#)
[Interactive Discussion](#)



**A numerical model
for volcanic jets**

S. Carcano et al.

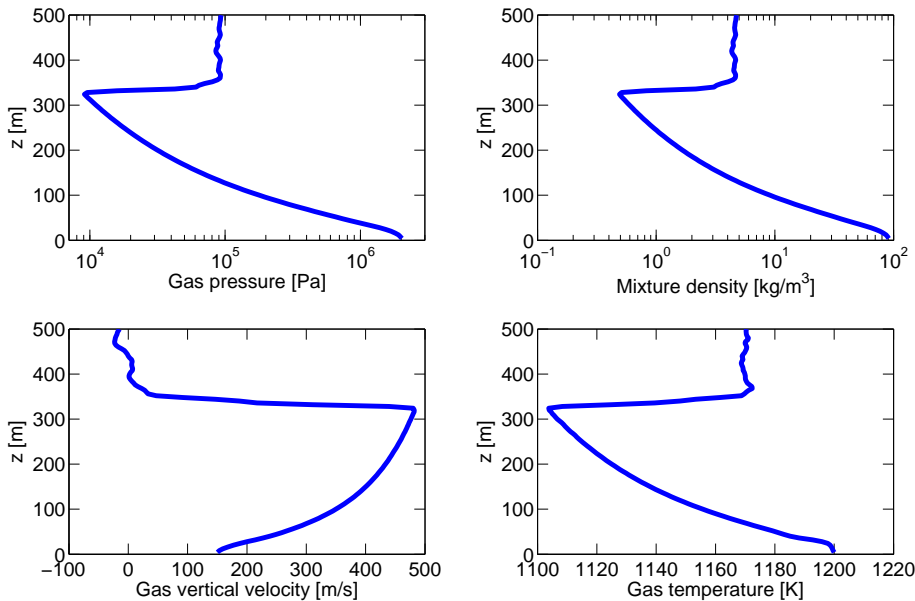


Fig. 9. Case A. Time-averaged axial profiles computed over the interval [16, 20] s of gas pressure, mixture density, gas vertical velocity and gas temperature.

[Title Page](#)[Abstract](#)[Introduction](#)[Conclusions](#)[References](#)[Tables](#)[Figures](#)[◀](#)[▶](#)[◀](#)[▶](#)[Back](#)[Close](#)[Full Screen / Esc](#)[Printer-friendly Version](#)[Interactive Discussion](#)

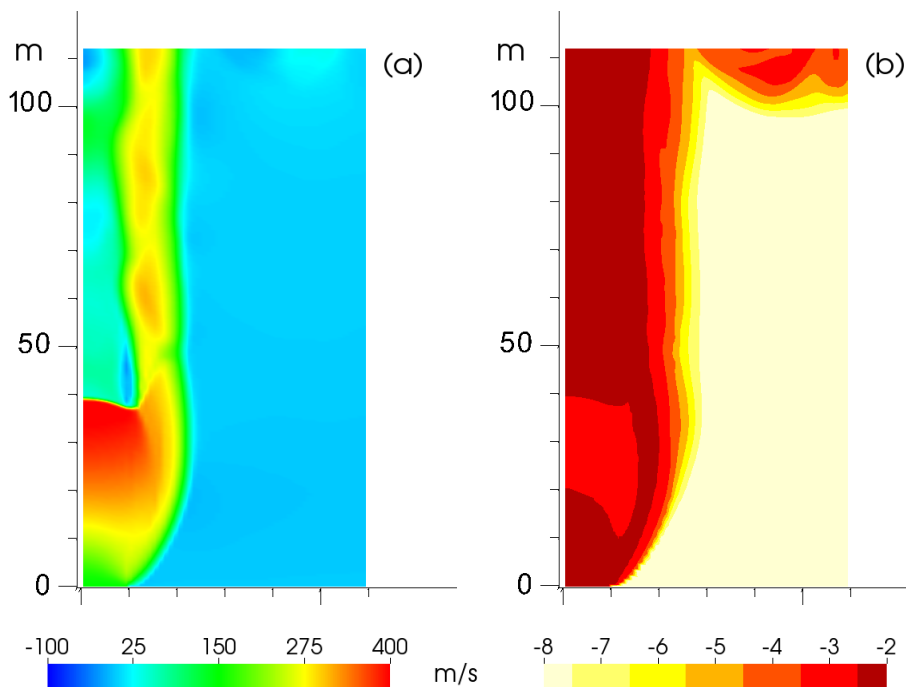


Fig. 10. Case B. **(a)** Gas vertical velocity [m s^{-1}] and **(b)** logarithm to the base 10 of particle volume fraction. Snapshots at $t = 2 \text{ s}$.

A numerical model for volcanic jets

S. Carcano et al.

Title Page

Abstract

Introduction

Conclusion

References

Tables

Figures

1

10

Back

Close

Full Screen / Esc

[Printer-friendly Version](#)

Interactive Discussion



A numerical model for volcanic jets

S. Carcano et al.

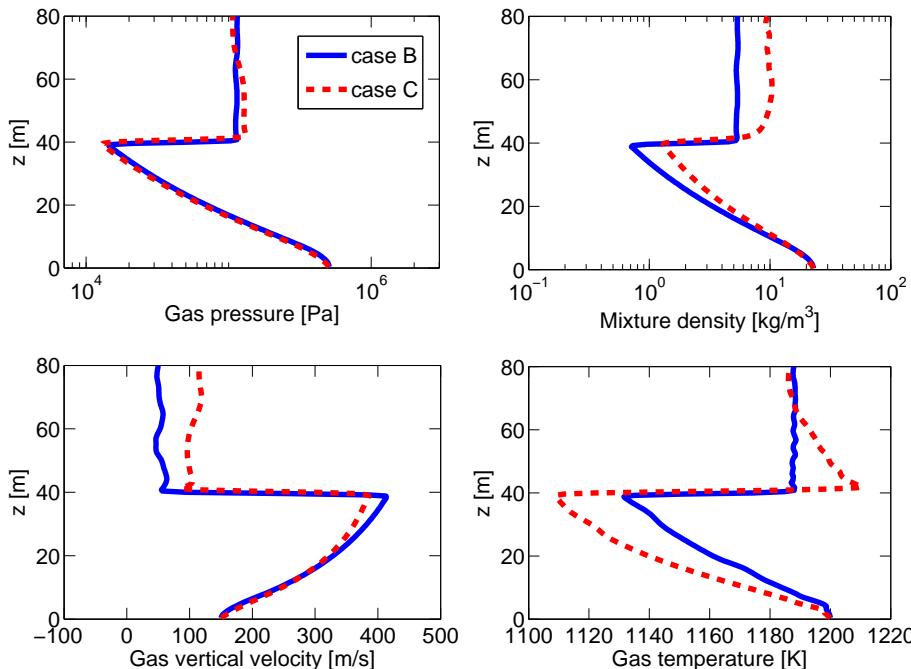


Fig. 11. Case B and C. Time-averaged axial profiles computed over the interval [1.6, 2.0] s of gas pressure, mixture density, gas vertical velocity and gas temperature.

[Title Page](#)

[Abstract](#)

[Introduction](#)

[Conclusions](#)

[References](#)

[Tables](#)

[Figures](#)

◀

▶

◀

▶

[Back](#)

[Close](#)

[Full Screen / Esc](#)

[Printer-friendly Version](#)

[Interactive Discussion](#)

A numerical model
for volcanic jets

S. Carcano et al.

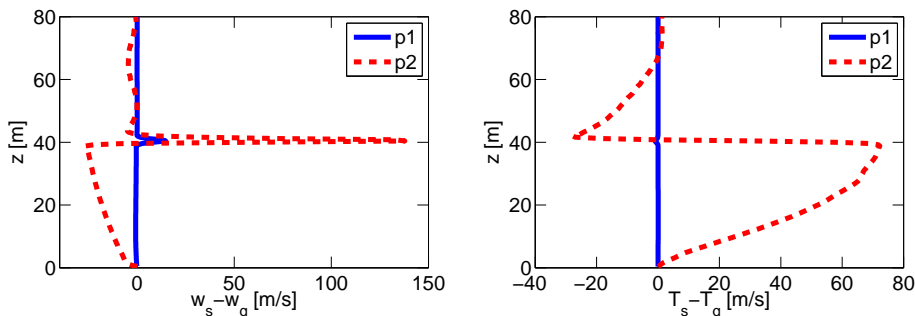


Fig. 12. Case C. Time averaged axial profiles of gas-particles mechanical and thermal non-equilibrium computed over the time interval [1.6, 2.0] s. Difference between gas vertical velocity and particle vertical velocities (left) and difference between gas temperature and particle temperatures (right).

[Title Page](#)[Abstract](#)[Introduction](#)[Conclusions](#)[References](#)[Tables](#)[Figures](#)[◀](#)[▶](#)[◀](#)[▶](#)[Back](#)[Close](#)[Full Screen / Esc](#)[Printer-friendly Version](#)[Interactive Discussion](#)

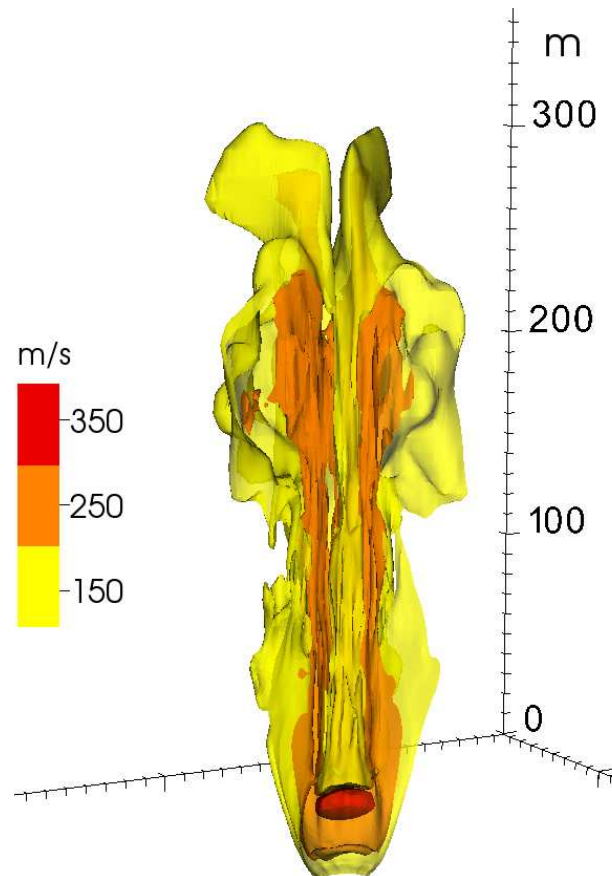


Fig. 13. Isosurfaces of gas vertical velocity [ms^{-1}] at $t = 2\text{ s}$.

450

 CC BY

Interactive Discussion

[Printer-friendly Version](#)

[Back](#)

1

Abstract Introduction

Conclusions References

Tables Figures

1

[Back](#)

Tables

Conclusions References

Title Page

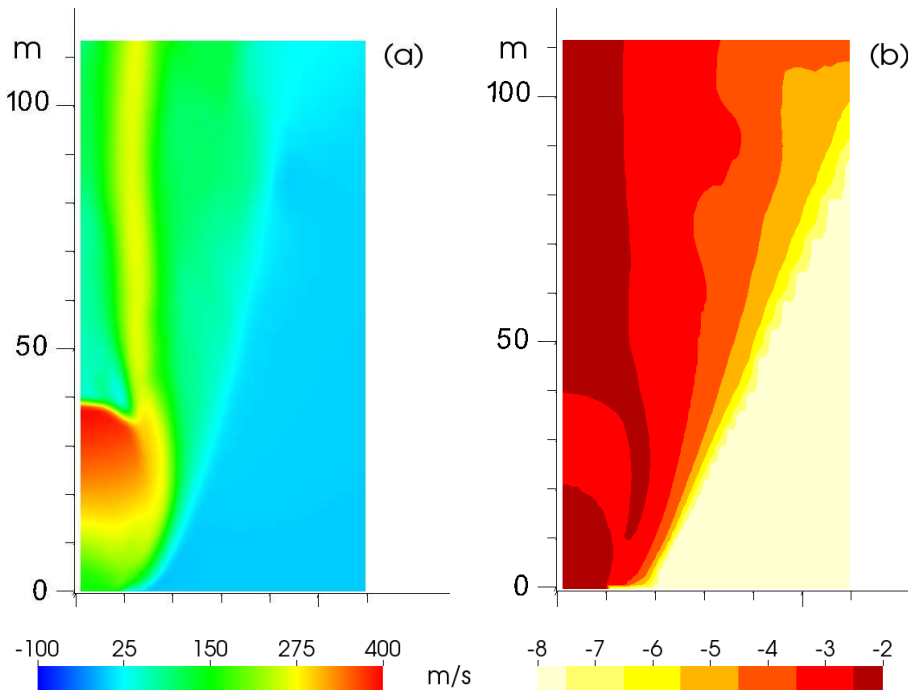


Fig. 14. (a) Gas vertical velocity [m s^{-1}] and **(b)** logarithm to the base 10 of particle volume fraction. Snapshots at $t = 2\text{ s}$ of a vertical section of averaged quantities along the azimuthal angle.

A numerical model for volcanic jets

S. Carcano et al.

Title Page

Abstract

Introduction

Conclusion

References

Tables

Figures

1

10

Back

Close

Full Screen / Esc

[Printer-friendly Version](#)

Interactive Discussion



A numerical model for volcanic jets

S. Carcano et al.

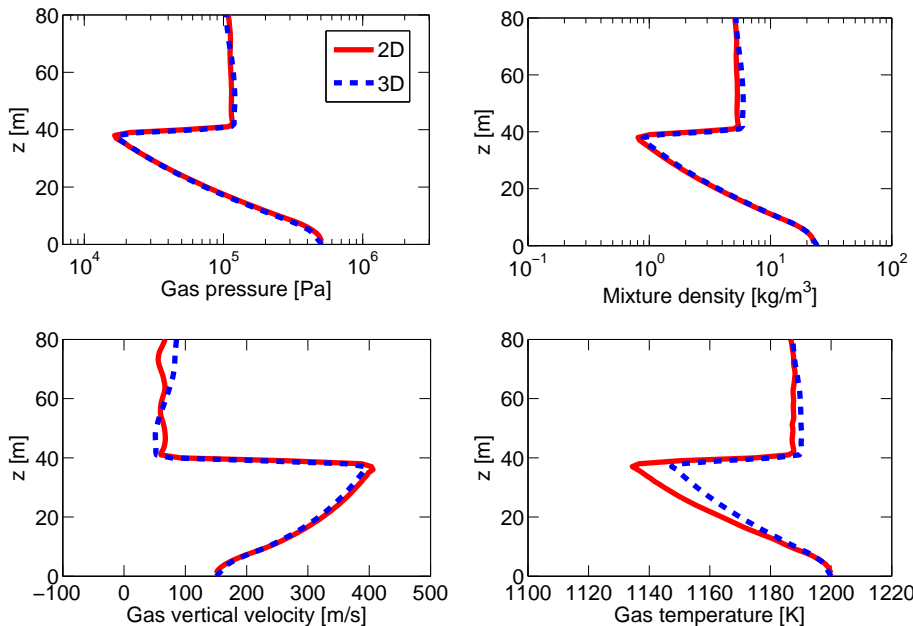


Fig. 15. Case B. Comparison between 2-D and 3-D simulations. Average axial profiles of gas pressure, gas vertical velocity, mixture density and gas temperature computed over the time interval [1.6, 2.0] s.

[Title Page](#)

[Abstract](#)

[Introduction](#)

[Conclusions](#)

[References](#)

[Tables](#)

[Figures](#)

[◀](#)

[▶](#)

[◀](#)

[▶](#)

[Back](#)

[Close](#)

[Full Screen / Esc](#)

[Printer-friendly Version](#)

[Interactive Discussion](#)